https://doi.org/10.5194/essd-2026-79
Preprint. Discussion started: 24 March 2026

Open Access Earth System Science Data Discussions

A global, spatially seamless, daily FY-3B soil moisture dataset based on a spatiotemporal deep learning model

Yanling You [a], Qunming Wang [a,*], Ronghan Xu [b,c,d,e], Xiaohua Tong [a]

[a] College of Surveying and Geo-Informatics, Tongji University, 1239 Siping Road, Shanghai 200092, China
[b] Key Laboratory of Radiometric Calibration and Validation for Environmental Satellites, National Satellite Meteorological Center (National Center for Space Weather), China Meteorological Administration, Beijing 100081, China
[c] Innovation Center for FengYun Meteorological Satellite (FYSIC), Beijing 100081, China
[d] Key Laboratory of Radiometric Calibration and Validation for Environmental Satellites, China Meteorological Administration, Beijing 100081, China
[e] Key Laboratory of Remote Sensing Application and Innovation, Chongqing Institute of Meteorological Sciences, Chongqing 401147, China
*Corresponding author. E-mail: wqm11111@126.com.

Abstract: The Fengyun-3B (FY-3B) satellite provides an effective platform for monitoring soil moisture (SM) from regional to global scales, and the produced SM data constitute an important component among various SM products. However, the Fengyun-3B (FY-3B) SM product contains a large number of missing data mainly due to orbital gaps, which significantly limit its applicability. To address this issue, a parallel spatiotemporal reconstruction model that integrates local fine-grained features and global semantic representations was proposed, called GSP (multi-scale Gated Convolution-residual Shifted Window Transformer Parallel) model. The GSP model fully utilizes the spatiotemporal information of FY-3B SM, and leverages the complementary modules to enhance spatiotemporal feature representation. Specifically, the multi-scale gated convolutions are applied to focus on the irregular valid pixels and extract multi-scale local spatiotemporal features, while the residual Shifted Window Transformer (Swin transformer) is leveraged to capture global spatiotemporal texture. Based on GSP, a global, spatially seamless, daily FY-3B SM dataset from 12 July 2011 to 19 August 2019 was generated. In the experiments, the model was evaluated with two strategies: 1) real gaps, where *in-situ* data at the same geographical locations were used as reference data, and 2) simulated gaps, where the original FY-3B SM data were masked by orbital gaps, and originally known data were used as reference. The results based on both strategies indicate that the GSP-reconstructed FY-3B SM data present greater accuracy than three typical reconstruction methods. The ubRMSE based on 17 sparse and five dense *in-situ* networks is 0.0703 m^3/m^3 and 0.0631 m^3/m^3, respectively. This dataset can be downloaded at https://doi.org/10.6084/m9.figshare.30633548 (You et al., 2026).

https://doi.org/10.5194/essd-2026-79
Preprint. Discussion started: 24 March 2026

Open Access Earth System Science Data Discussions

1. Introduction

Soil moisture (SM) is an essential variable that impacts the hydrological balance and atmospheric feedback (Lei et al., 2022). It is also an important component of the water cycle in terrestrial ecosystems and has been widely applied in fields such as climate modeling (Berg and Mulroy, 2006; Koster et al., 2004) and drought monitoring (Ford and Quiring, 2019; Zhang et al., 2016). Conventional *in-situ* measurements can provide ground-based SM data with very high temporal resolution and accuracy, which have been commonly used to evaluate simulated SM at different spatial and temporal scales (Long et al., 2019b). Nevertheless, the sparse distribution of ground stations hinders the temporal and spatial continuous observations of SM, significantly restricting its applications at the global scale (Qin et al., 2017; Xing et al., 2017; Owe et al., 2008). Although the land surface models are capable of providing spatially and temporally continuous SM observations, the accuracy is often limited by uncertainties in model parameters and structural design (Shangguan et al., 2023). Satellite remote sensing, especially microwave remote sensing, has been considered as an effective solution for SM retrieval due to its strong penetration ability and sensitivity to near-surface SM.

The distinctive advantages of microwave remote sensing in SM retrieval have accelerated the development of global SM products. Numerous active and passive microwave satellites have been deployed to monitor SM. Active microwave sensors include the NASA-ISRO SAR Mission (NISAR) (Kellogg et al., 2020), Advanced Scatterometer (ASCAT) (Bartalis et al., 2007), Sentinel-1 (Davidson et al., 2009), and WindRAD onboard China's meteorological satellite FengYun-3E (FY-3E/WindRAD) (Li et al., 2023). Passive microwave sensors include the Scanning Multichannel Microwave Radiometer (SMMR) (Njoku et al., 1980), Special Sensor Microwave Imager (SSM/I) (Hollinger et al., 1991), Tropical Rainfall Measuring Mission (TRMM) (Simpson et al., 1996), Advanced Microwave Scanning Radiometer-EOS (AMSR-E) (Kawanishi, 2003), Microwave Radiation Imager onboard FengYun-3B (FY-3B/MWRI) (Yang et al., 2011), Soil Moisture and Ocean Salinity (SMOS) (Kerr et al., 2010), and Advanced Microwave Scanning Radiometer 2 (AMSR2) (Parinussa et al., 2015). Additionally, the Soil Moisture Active and Passive (SMAP) mission integrates both active and passive sensors for global SM observation (Entekhabi et al., 2009).

The FY-3B satellite was equipped with a highly sensitive passive microwave radiometer (MWRI), which has exhibited the ability to capture the dynamics of SM at both global and regional scales (Parinussa et al., 2017). Parinussa et al. (2014) applied the Land Parameter Retrieval Model (LPRM) to the observations of MWRI and compared the SM estimates with the official FY-3B SM products, demonstrating that both products accurately captured the temporal variations of SM, with correlation coefficients (R) exceeding 0.60. However, there exist noticeable gaps due to several factors, including discontinuous satellite orbital coverage, sensor limitations, radio-frequency interference, and frozen soil, resulting in a large number of data losses at the global scale (Llamas et al., 2020). Such discontinuities significantly affect the application of FY-3B SM, particularly for spatial pattern analysis at a daily scale. Fig. 1 shows the temporal coverage proportion of FY-3B SM at the global scale from 12 July 2011 to 19 August 2019. It is seen that the proportion varies spatially, with particularly severe gaps observed in high latitude areas. Therefore, there is a great need to reconstruct a spatiotemporally continuous FY-3B SM dataset to substantially enhance the application value of FY-3B SM products.

https://doi.org/10.5194/essd-2026-79
Preprint. Discussion started: 24 March 2026

Open Access Earth System Science Data Discussions

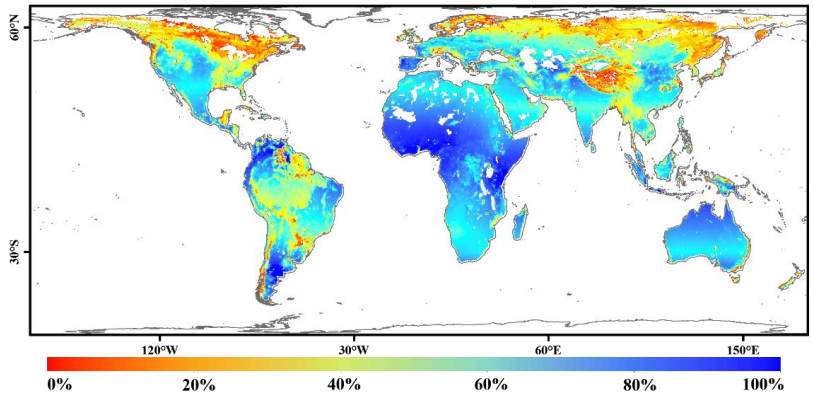

Fig. 1. The temporal coverage proportion of FY-3B SM at the global scale from 12 July 2011 to 19 August 2019.

Deep learning has been widely applied in the reconstruction of SM, due to its powerful nonlinear modeling and automatic feature extraction capabilities. Additionally, auxiliary data generally play a critical role in SM reconstruction, where they can be categorized into heterogeneous and homogeneous data. The strategy for reconstructing SM based on heterogeneous data involves deriving various driving variables from external sensors and establishing statistical or physical relationships between these variables and SM. Common examples include Land surface temperature (LST), Normalized Difference Vegetation Index (NDVI), precipitation, Digital Elevation Model (DEM), and soil physical properties, as they are capable of characterizing land–atmosphere interactions and show strong spatiotemporal associations with SM (Long et al., 2019a). For example, Zhang et al. (2023) integrated a series of heterogeneous auxiliary data, including precipitation, temperature, wind speed, and land cover type, and proposed a spatiotemporal deep learning model for SM prediction. Fang et al. (2017) developed a deep learning-based prediction system for the SMAP L3 SM product using atmospheric forcing and static topographic attributes as inputs. Shangguan et al. (2023) employed NDVI, LST, and DEM to develop a residual deep neural network with spatiotemporal attention and fill the gaps in the Climate Change Initiative program of the European Space Agency (ESA CCI) SM dataset over the Tibetan Plateau from 2001 to 2021.

In addition to inherent orbital gaps, heterogeneous auxiliary data derived from optical sensors are also susceptible to widespread data gaps resulting from cloud contamination, which limits the reconstruction methods to clear-sky conditions (Jing et al., 2018). Moreover, the above methods mainly rely on the statistical correlation between heterogeneous auxiliary data and SM. However, discrepancies in their physical meanings inevitably affect the reliability of model fitting (Tavakol et al., 2019).

To overcome these limitations, an increasing number of studies have considered using homogeneous information from SM itself to provide more reliable data support for SM reconstruction. The homogeneous information includes spatial information, temporal information, and an integration of both. For spatial information, missing data often exhibit contextual consistency and spatial correlation with spatially adjacent data (Shen et al., 2015). For example, Hegazi et al. (2021) predicted missing agricultural SM with a convolutional neural network (CNN)

https://doi.org/10.5194/essd-2026-79
Preprint. Discussion started: 24 March 2026

architecture. From the perspective of temporal information, reconstruction mainly relies on capturing both short-term dynamic variability and long-term temporal patterns in time series data. Li et al. (2022) proposed a novel causality-based long short-term memory (CLSTM) model to learn temporal correlations and causal relationships within SM datasets. Wang et al. (2025) proposed the Temporal Convolutional Network (TCN)-Transformer Parallel (TTP) model to extract the partial and global features of annual time series. Actually, both spatial and temporal information are critical for SM reconstruction, and it has become a new trend to effectively extract their features simultaneously (spatiotemporal information). Convolutional Neural Network (CNN) is capable of capturing mid- and high-level abstract features from a spatiotemporal cube, automatically learning texture and structural features, and maintaining high compatibility with other modules (e.g., attention mechanisms and residual connections) (Zhu et al., 2018). Vanilla convolutions in CNN assume that all pixels in the input image are valid and extract local features through a sliding window. Thus, in reconstruction tasks, applying convolutions that treat valid and invalid pixels equally, the results will be affected by invalid values (Liu et al., 2018). This often leads to visual artifacts such as color discrepancy, blurriness, and obvious edge responses.

To enhance the applicability of convolutions for data reconstruction, partial convolutions introduce a binary mask (i.e., valid pixels as 1 and invalid pixels as 0) to ensure the convolutions and normalizations are applied exclusively to valid pixels (Liu et al., 2018). In each layer, the distribution of valid pixels within the mask is updated through a mask update step, thereby enabling more effective handling of incomplete data inputs. Partial convolutions have also been widely applied to the spatiotemporal reconstruction of SM. For example, Zhang et al. (2021) developed a new three-dimensional spatiotemporal partial CNN and generated a seamless global daily SM (SGD-SM) dataset from 2013 to 2019. Subsequently, a long short-term memory (LSTM) network was integrated with the partial convolutions to further extract spatiotemporal features of SM, resulting in the SGD-SM 2.0 dataset (Zhang et al., 2022). Wei et al. (2024) applied a partial CNN to extract spatial features from SM and produced a global daily seamless SM dataset from 2015 to 2022.

Nevertheless, partial convolution employs a fixed-rule mask update mechanism in which as long as there is at least one valid pixel within the filter range of the previous layer, the corresponding mask value in the next layer will be set to 1. This prevents the model from adaptively determining the validity of features. Additionally, the discrete mask update process often causes invalid pixels to disappear in the deeper layers (Chang et al., 2020). Moreover, the mask is shared across channels, limiting the capacity for channel-specific modeling. To deal with this issue, gated convolution was developed (Yang et al., 2024). Specifically, by introducing a learnable dynamic feature selection mechanism for each spatial location in each channel across all layers, gated convolution can adaptively assess the feature validity at both channel and spatial dimensions. In contrast to hard masks of partial convolution, the weights in gated convolution are continuous, which can reduce boundary artifacts and abrupt texture changes (Dai et al., 2020). Gated convolution adaptively selects features for irregularly missing data, effectively extracting locally valid features and demonstrating substantial potential for missing data reconstruction.

While gated convolution demonstrates capability in local texture extraction, its ability to model long-range dependencies and global relationships is limited by the inherent receptive field of convolution operations. In contrast, the recently developed Shifted Window Transformer (Swin Transformer) can capture more accurate global features. Specifically, the Swin Transformer adapts

https://doi.org/10.5194/essd-2026-79
Preprint. Discussion started: 24 March 2026

the global interaction capability of the Transformer from sequence modeling to vision by a shifted window strategy (Xu et al., 2024). With this strategy, it accounts for interactions among pixels across different windows and effectively captures global contextual information. This architecture has been widely applied in various tasks, including object detection (Zhang et al., 2024c) and semantic segmentation (Zhang et al., 2024a). Therefore, the Swin Transformer with a shifted window self-attention mechanism can compensate for gated convolution through hierarchical global modeling, and the joint use can potentially achieve collaborative optimization between local details and global texture.

In this paper, a new spatiotemporal reconstruction model was proposed, named GSP (multi-scale Gated Convolution-residual Shifted Window Transformer Parallel) model. This model integrates multi-scale gated convolutions, the residual Swin Transformer, and the Convolutional Block Attention Module (CBAM) to extract effective spatiotemporal features. The GSP model fully exploits multi-scale gated convolutions and the residual Swin Transformer to extract both local and global spatiotemporal features. Based on this model, a global, spatially seamless, daily FY-3B SM dataset from 12 July 2011 to 19 August 2019 was generated. The main contributions of this study are summarized as follows:

1) The GSP model was proposed to fill the data gaps in FY-3B SM. Based on the parallel network architecture, the two branches of the GSP model share inputs but independently extract the local and global features of the spatiotemporal information of FY-3B SM. Specifically, the multi-scale gated convolutions can capture local spatiotemporal features at different scales, and the residual Swin Transformer achieves global spatiotemporal interactions by window-based multi-head self-attention (W-MSA) and shifted window multi-head self-attention (SW-MSA). Additionally, the CBAM is incorporated to adaptively emphasize key information through channel and spatial attention mechanisms, thereby integrating local and global representations.
2) Based on the GSP model, a global, spatially seamless, daily FY-3B SM dataset from 12 July 2011 to 19 August 2019 was generated. Compared with the datasets produced by other reconstruction methods, the developed dataset demonstrates greater accuracy and provides more realistic spatial texture information.

2. Data

2.1 FY-3B SM

The FY-3B satellite was launched by the China National Space Administration (CNSA) on 5 November 2010. It was equipped with an MWRI for observing the Earth's surface (Geng et al., 2022; Cui et al., 2017). The MWRI operates across a frequency range from 10.7 GHz to 89 GHz and acquires data during both descending and ascending passes at local equator crossing times of approximately 1:40 AM and 1:40 PM, respectively (Liu et al., 2016; Wang et al., 2022). In this study, the daily FY-3B Level-2 SM product (with a spatial resolution of 25 km) were obtained from the National Satellite Meteorological Center, which provides publicly available data from 12 July 2011 to 19 August 2019. The data from ascending and descending orbits were composited for each day.

https://doi.org/10.5194/essd-2026-79
Preprint. Discussion started: 24 March 2026

Open Access Earth System Science Data Discussions

2.2 In-situ data

The *in-situ* SM data acquired through the International Soil Moisture Network (ISMN) were employed to validate the seamless FY-3B SM dataset reconstructed by GSP. ISMN collected globally distributed *in-situ* SM measurements, coordinated by the European Space Agency (ESA) and supported by numerous voluntary contributions from researchers and organizations worldwide (Dorigo et al., 2021). The data are publicly available at https://ismn.earth/en/. Considering that passive microwave radiometers cannot penetrate deeper soil layers, the depth of all selected *in-situ* observations in this study was smaller than 0.05 m to ensure consistency with the measured depth of the FY-3B SM (Dorigo et al., 2013). The detailed information of the *in-situ* data used will be provided in Section 3.3.

2.3 Köppen-Geiger climate classification data

The Köppen-Geiger climate classification data divides climates into five major categories and 30 subtypes, defined by monthly temperature and precipitation thresholds in combination with seasonal features. Beck et al. (2018) have provided the global maps of Köppen-Geiger climate classification at 1 km spatial resolution for the present and future conditions, which are accessible at www.gloh2o.org/koppen. In this study, the present Köppen-Geiger classification was employed and resampled to 25 km to evaluate the reconstruction performance across different climate types.

3. Methods

3.1 Overview

The training and prediction workflow based on the proposed GSP model is shown in Fig. 2. The FY-3B SM data from 16 July 2011 to 31 December 2016 were employed as the training dataset, while the FY-3B SM data from 1 January 2017 to 15 August 2019 were used as the testing dataset for independent evaluation of the reconstruction performance. To reconstruct FY-3B SM for a given date T, spatiotemporal data from nine consecutive days (from $T-4$ to $T+4$) are first selected, and a binary mask is generated based on invalid pixel flags. Training samples are created through patch selection and simulated mask generation. The testing samples were generated using the same procedure to ensure consistency in the data preparation process. During patch selection, the geographical location with spatially complete patches (with a spatial size of 40×40 pixels) at T is considered. The spatiotemporal data (from $T-4$ to $T+4$) are subsequently organized into the patch groups (with the size of 40×40×9). Then, the simulated mask (extracted from real orbital gaps in FY-3B SM) is applied to the spatially complete patch at T to simulate the missing patterns as closely as possible. Specifically, the global FY-3B SM masks from 12 July 2011 to 19 August 2019 are traversed, and mask patches (with the spatial size of 40×40) with missing rates between 30 % and 70 % are selected. The spatiotemporal patch groups (from $T-4$ to $T+4$) with simulated gaps at T are used as input features of training data. The originally known data under the mask at T are used as the corresponding training labels. The samples collected from all dates from 16 July 2011 to 31 December 2016 are used together to train the learning model.

During model training, the Euclidean distance is used as the loss function. The loss between

https://doi.org/10.5194/essd-2026-79
Preprint. Discussion started: 24 March 2026

Open Access Earth System Science Data Discussions

predicted and originally known FY-3B SM within the simulated masked regions is calculated, and its gradient is propagated to the optimizer through gradient descent to iteratively update the model parameters. The formulas of the loss function are as follows:

$$M_n = \begin{cases} 1, & if\ X_n\ is\ masked \\ 0, & otherwise \end{cases} \#(1)$$

$$Loss(\mathbf{X}, \widehat{\mathbf{X}}, \mathbf{M}) = \frac{\sum_{n=1}^{N} \left((\hat{X}_n - X_n) \odot M_n \right)^2}{\sum_{n=1}^{N} M_n} \#(2)$$

where $\mathbf{M}$ represents the simulated mask matrix, with 1 representing masked and 0 not. M_n indicates the value of $\mathbf{M}$ at location n. $\mathbf{X}$ represents the original spatially complete FY-3B SM patch, and $\widehat{\mathbf{X}}$ represents the reconstructed spatially complete FY-3B SM patch. X_n and $\hat{X}_n$ represent the original and reconstructed values of FY-3B SM at location n, respectively.

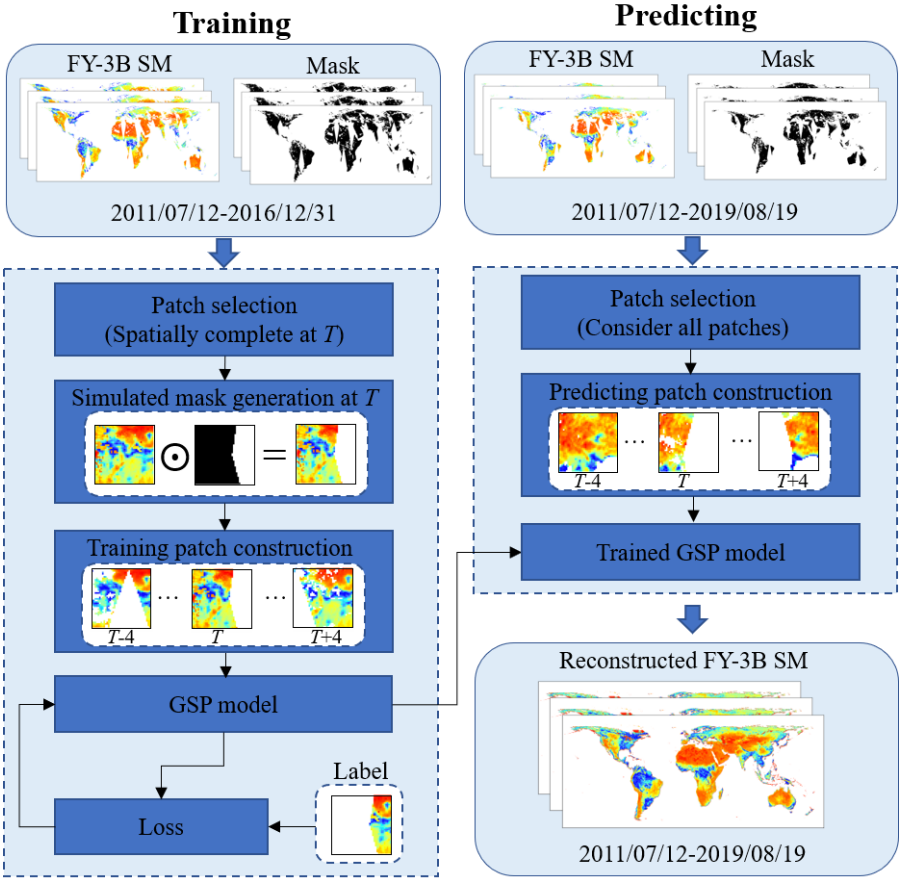

Fig. 2. The proposed GSP-based training and predicting workflow.

During prediction, for each day, the spatiotemporal patches from nine temporally closest days (with the same size of 40×40×9 as training data) for locations with real orbital gaps. The spatiotemporal patches are then input into the trained GSP model to produce seamless patches,

https://doi.org/10.5194/essd-2026-79
Preprint. Discussion started: 24 March 2026

Open Access Earth System Science Data Discussions

which are then stitched together to generate the spatially complete FY-3B SM dataset on each date from 12 July 2011 to 19 August 2019. It should be noted that, for the special case of periods without sufficient earlier (or later) FY-3B SM data, that is, form 12 July 2011 to 15 July 2011 (16 August 2019 to 19 August 2019), the FY-3B SM data from T to $T+4$ (form $T-4$ to T) are used as input for the model (i.e., treat the data from $T-4$ to $T-1$ (form $T+1$ to $T+4$) as completely missing data).

3.2 GSP architecture

As shown in Fig. 3, the model consists of three main components, including the multi-scale gated convolution block, the residual Swin Transformer block, and the feature fusion block. The multi-scale gated convolutions block and residual Swin Transformer block are organized in a parallel architecture to extract local and global spatiotemporal features, respectively. The extracted features are then concatenated and fed into the fusion block to fully exploit both types of features. The fusion module includes the CBAM and multiple convolutional layers. Residual connections are incorporated to transfer features from previous layers to subsequent layers, thereby mitigating the problem of gradient vanishing. Furthermore, to enhance the spatial coverage of the initial reference data and incorporate more reliable FY-3B SM information from temporally neighboring data, the four-month temporal average of FY-3B SM at each location is introduced into the feature fusion block as the initial input to mitigate the effect of large-scale data gaps on FY-3B SM reconstruction.

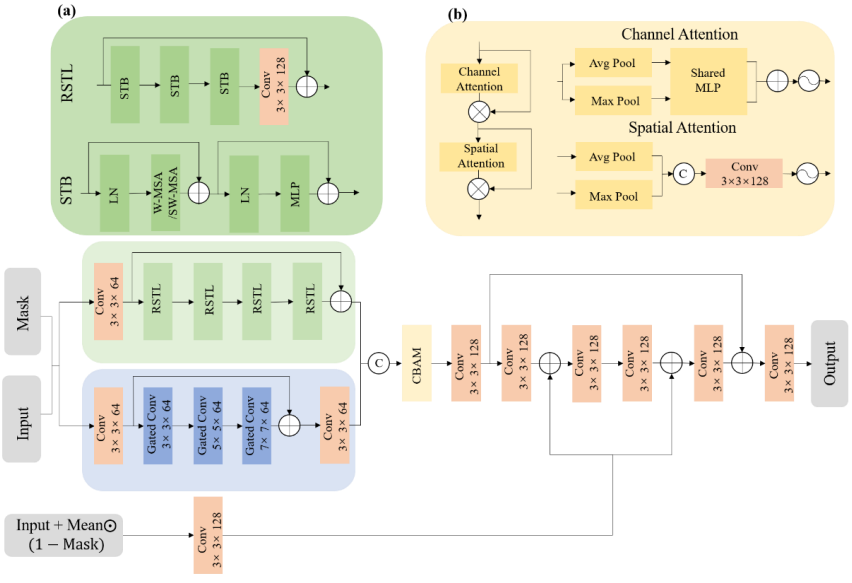

Fig. 3. The architecture of the GSP model. The blue box represents the multi-scale gated convolution block, and the green box represents the residual Swin Transformer block. (a) is the architecture of the residual Swin Transformer layer (RSTL), and (b) represents the CBAM ("STB" represents the Swin Transformer block, "LN" is the abbreviation for "Layer Normalization",

https://doi.org/10.5194/essd-2026-79
Preprint. Discussion started: 24 March 2026

"W-MSA" and "SW-MSA" represent window-based multi-head self-attention and shifted window multi-head self-attention, respectively, and MLP represents the multilayer perceptron. "Conv" represents the convolution operation, "Avg Pool" represents the average pooling, and "Max Pool" represents the max pooling).

3.2.1 Multi-scale gated convolution block

To mitigate the limitations of hard mask updated rules of partial convolutions, gated convolutions are introduced to improve the reconstruction performance under irregular missing data. Unlike partial convolution, the gated convolutions can learn an automatically soft mask from data and adaptively adjust the output features according to the soft mask, thereby more effectively focusing on irregular valid pixel regions (Yang et al., 2024). Additionally, to capture features from different receptive field scales, the multi-scale gated convolution block (see the blue box in Fig. 3) is designed with three kernels of varying sizes (3×3, 5×5, and 7×7), enabling the model to integrate multi-scale spatiotemporal information. The specific implementation is as follows:

$$Gating_{t,x,y} = \sum\sum W_g \cdot F_{t,x,y} \#(3)$$

$$Features_{t,x,y} = \sum\sum W_f \cdot F_{t,x,y} \#(4)$$

$$Output_{t,x,y} = \sigma\left(Gating_{t,x,y}\right) \odot \emptyset\left(Features_{t,x,y}\right) \#(5)$$

where $Gating_{t,x,y}$ and $Features_{t,x,y}$ represent the soft mask and feature value, respectively. $F_{t,x,y}$ and $Output_{t,x,y}$ represents the input feature and output feature, respectively. The subscript t,x,y is the spatial-temporal coordinate. W_g and W_f are the gating and feature convolutional filters. σ is the sigmoid function to transform $Gating_{t,x,y}$ to values between 0 (invalid) and 1 (valid), and $\emptyset$ is the activation function (i.e., LeakyReLU) (Yang et al., 2024).

3.2.2 Residual Swin Transformer block

The residual Swin Transformer block (see the green box in Fig. 3) is composed of multiple residual Swin Transformer layers (RSTL). Each RSTL consists of several Swin Transformer blocks (STB) combined with residual connections. With each RSTL, multiple STBs are stacked, and their outputs are subsequently processed by a convolutional layer. A residual connection is applied between the input and output to effectively integrate features across different layers.

The RSTL is a hierarchical vision transformer architecture designed to efficiently model visual data with varying scales (see (a) in Fig. 3). The input data are first divided into non-overlapping fixed-size patches through patch partitioning. Each patch is embedded into a feature vector through a linear transformation, forming the initial token sequence. Between successive STBs, patch merging operations are applied to merge neighboring patches, progressively reducing spatial resolution and increasing channel dimensions to construct multi-scale feature representations (Liu et al., 2021).

As shown in (a) in Fig. 3, each STB is composed of two layer normalizations (LN), a multi-head self-attention (MSA) mechanism (either W-MSA or SW-MSA), and a multilayer perceptron (MLP). LN is applied before each MSA and MLP, while residual connections are incorporated to enhance model stability (Tang et al., 2024). In contrast to global self-attention,

https://doi.org/10.5194/essd-2026-79
Preprint. Discussion started: 24 March 2026

which is computationally intensive, W-MSA performs computation in local windows, thereby reducing complexity. To facilitate information exchange across windows, SW-MSA is introduced between adjacent Transformer blocks (Xie et al., 2023). By shifting the window positions in successive layers, tokens within one window are able to interact with tokens in neighboring windows from the previous layer, enabling effective cross-window communication (Li et al., 2024b). This study used four RSTLs, each containing three STBs, with a window size of 4 for each STB. The implementation details are as follows:

$$\mathbf{Z}_{\mathbf{l}}^{'} = \mathrm{W\_MSA}\left(\mathrm{LN}(\mathbf{Z}_{\mathbf{l-1}})\right) + \mathbf{Z}_{\mathbf{l-1}} \#(6)$$

$$\mathbf{Z}_{\mathbf{l}} = \mathrm{MLP}\left(\mathrm{LN}\left(\mathbf{Z}_{\mathbf{l}}^{'}\right)\right) + \mathbf{Z}_{\mathbf{l}}^{'} \#(7)$$

$$\mathbf{Z}_{\mathbf{l+1}}^{'} = \mathrm{SW\_MSA}\left(\mathrm{LN}(\mathbf{Z}_{\mathbf{l}})\right) + \mathbf{Z}_{\mathbf{l}} \#(8)$$

$$\mathbf{Z}_{\mathbf{l+1}} = \mathrm{MLP}\left(\mathrm{LN}\left(\mathbf{Z}_{\mathbf{l+1}}^{'}\right)\right) + \mathbf{Z}_{\mathbf{l+1}}^{'} \#(9)$$

where $\mathbf{Z}_{\mathbf{l}}^{'}$ (or $\mathbf{Z}_{\mathbf{l+1}}^{'}$)and $\mathbf{Z}_{\mathbf{l}}$ (or $\mathbf{Z}_{\mathbf{l+1}}$) denote the output features of the W-MSA (or SW-MSA) and MLP modules for block l, respectively; W_MSA and SW_MSA denote window-based multi-head self-attention using regular and shifted window partitioning configurations, respectively. LN represents the Layer Normalization.

3.2.3 CBAM

The CBAM is a lightweight attention mechanism that automatically focuses on important channel features and key spatial locations by sequentially combining channel and spatial attention mechanisms (see (b) in Fig. 3) (Woo et al., 2018). The channel attention mechanism emphasizes informative channels by applying parallel max pooling and average pooling to compress the feature map along the spatial dimension, after which a shared MLP is used to compute the channel attention map. The spatial attention mechanism similarly compresses the feature map along the channel dimension using max pooling and average pooling, generating the spatial attention map through convolution (Zhang et al., 2024b). The input is weighted by the channel and spatial attention maps in sequence to produce more reliable feature representations.

3.3 Validation Strategy

Two deep learning models for spatiotemporal data reconstruction were selected for comparison. The first model, named U-TILISE, integrates convolutional U-Net layers in spatial dimensions with Transformer layers in the temporal dimension to implicitly capture spatiotemporal patterns of input data (Stucker et al., 2023). The second, the spatiotemporal model with partial convolutions (STpconv), combines 3D spatiotemporal partial convolutions with a U-Net architecture to reconstruct data gaps in satellite SM (Appel, 2024). Additionally, a penalized least square regression model based on three-dimensional discrete cosine transform (DCT-PLS) was also implemented for comparison, which explicitly utilizes information from both spatial and temporal dimensions to predict the missing values (Zhang et al., 2016; Wang et al.,

https://doi.org/10.5194/essd-2026-79
Preprint. Discussion started: 24 March 2026

2012).

The FY-3B SM dataset (from 12 July 2011 to 19 August 2019), reconstructed based on GSP, was evaluated using the network-level *in-situ* data, which have been widely recognized as references for SM validation. This evaluation validates whether the reconstruction can represent the original FY-3B SM at corresponding locations. Meanwhile, to minimize the effects of differences in spatial locations of stations, all networks were divided into two types according to the distribution of stations, including sparse (i.e., stations are distributed within different pixels) and dense (i.e., all stations are distributed within only one pixel) *in-situ* data. Fig. 4 and Table 1 present the spatial distribution and details of the two types of *in-situ* networks used in this study, including 17 sparse networks and five dense networks. Moreover, to further examine the GSP model, reconstruction performances under simulated gaps were also considered for evaluation, with the originally known data as a perfect reference. Similar to the simulated mask process during training, the real missing patterns in FY-3B SM were applied to simulate partial spatial gaps to evaluate the GSP performance under different proportions of spatial missing (i.e., 30 %-70 %). Four accuracy evaluation metrics were used, including *R*, root mean square error (RMSE), mean absolute error (MAE), and unbiased RMSE (ubRMSE).

Table 1

Basic information of the *in-situ* networks used for validation.

Types	Network	Number of stations	Location (country)	Period (yyyy/mm/dd)
Sparse	**AMMA-CATCH**	7	Benin, Niger, Mali	2006/01/01 to 2018/12/31
	ARM	35	USA	1993/06/29 to 2025/12/14
	CTP_SMTMN	57	China	2010/08/01 to 2016/09/19
	MAQU	27	China	2008/05/13 to 2019/06/01
	NAQU	11	China	2010/06/15 to 2019/09/12
	ORACLE	6	France	1985/10/18 to 2013/09/09
	OZNET	38	Australia	2001/09/12 to 2021/09/01
	PBO_H2O	163	USA	2004/09/27 to 2017/12/16
	REMEDHUS	24	Spain	2005/03/15 to 2025/01/01
	SCAN	222	USA	1996/08/15 to 2025/12/16
	SMN-SDR	34	China	2018/07/25 to 2019/12/31
	SNOTEL	509	USA	1996/09/10 to 2025/12/16
	SOILSCAPE	224	USA	2011/08/03 to 2025/12/16
	TAHMO	70	Côte d'Ivoire, Nigeria, Ghana, Uganda, Rwanda, Kenya	2015/06/17 to 2022/07/07
	TxSON	41	USA	2014/10/01 to 2022/11/08
	USCAN	115	USA	2000/11/15 to 2025/12/16
	XMS-CAT	20	Spain	2016/08/01 to 2025/12/16
Dense	**BIEBRZA_S-1**	30	Poland	2015/04/23 to 2018/12/01
	Ru_CFR	2	Russia	2015/05/25 to 2024/12/31
	SD_DEM	1	Sudan	2002/02/08 to 2020/11/12

https://doi.org/10.5194/essd-2026-79
Preprint. Discussion started: 24 March 2026

	SWEX_POLAND	6	Poland	2000/01/01 to 2013/05/06
	VAS	3	Spain	2010/01/01 to 2012/01/01

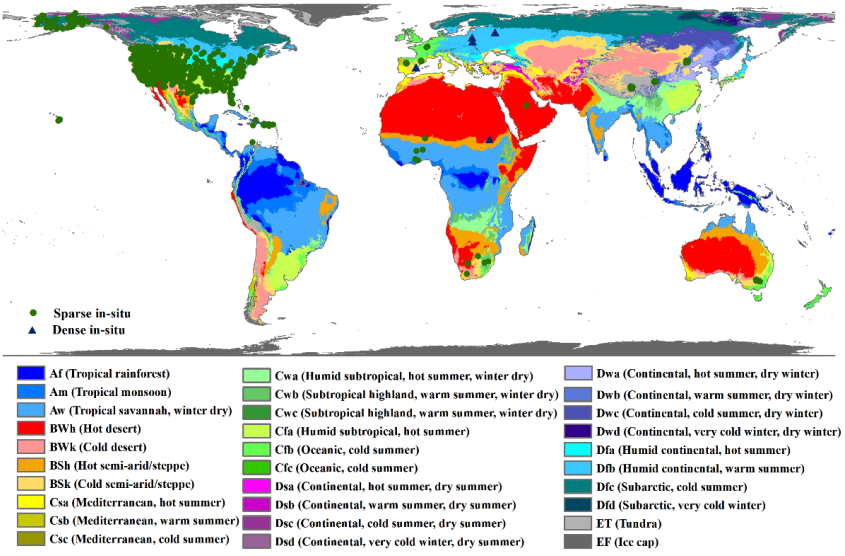

Fig. 4. Spatial distribution of the *in-situ* data used for validation, with the green points and blue triangles representing the *in-situ* stations in the sparse and dense networks, respectively (the Köppen-Geiger climate classification data were used as the base map).

4. Results

4.1 Validation with in-situ data

In the validation based on the *in-situ* data at the sparse networks, the 17 sparse networks were used to evaluate the accuracy of the seamless FY-3M dataset generated by different methods. As shown in Fig. 5, the temporal dynamics of all reconstructed FY-3B SM datasets are generally consistent with *in-situ* data. Among them, the reconstruction based on GSP is the closest to the *in-situ* data, which effectively captures the interannual variation in FY-3B SM. In contrast, the reconstruction based on U-TILISE tends to underestimate FY-3B SM at some networks, such as CTP_SMTMN and MAQU. The DCT-PLS-based reconstruction displays inconsistent and dispersed temporal patterns in several networks (e.g., SNOTEL and XMS-CAT).

Table 2 presents the quantitative evaluation results across the 17 sparse networks. It is seen that the reconstructed FY-3B SM based on GSP consistently outperforms the other methods in all four metrics. It achieves the largest mean *R* of 0.5387, which is 0.1000, 0.0634, and 0.0037 larger than those of U-TILISE, STpconv, and DCT-PLS, respectively. Its mean ubRMSE is 0.0703 m ³/m ³, which is 0.0131 m ³/m ³, 0.0092 m ³/m ³, and 0.0025 m ³/m ³lower than the corresponding values for the other three methods. Particularly at the TAHMO network, the GSP-based reconstruction achieves the smallest RMSE and MAE of 0.0448 m ³/m ³and 0.0371 m ³/m ³, respectively.

https://doi.org/10.5194/essd-2026-79
Preprint. Discussion started: 24 March 2026

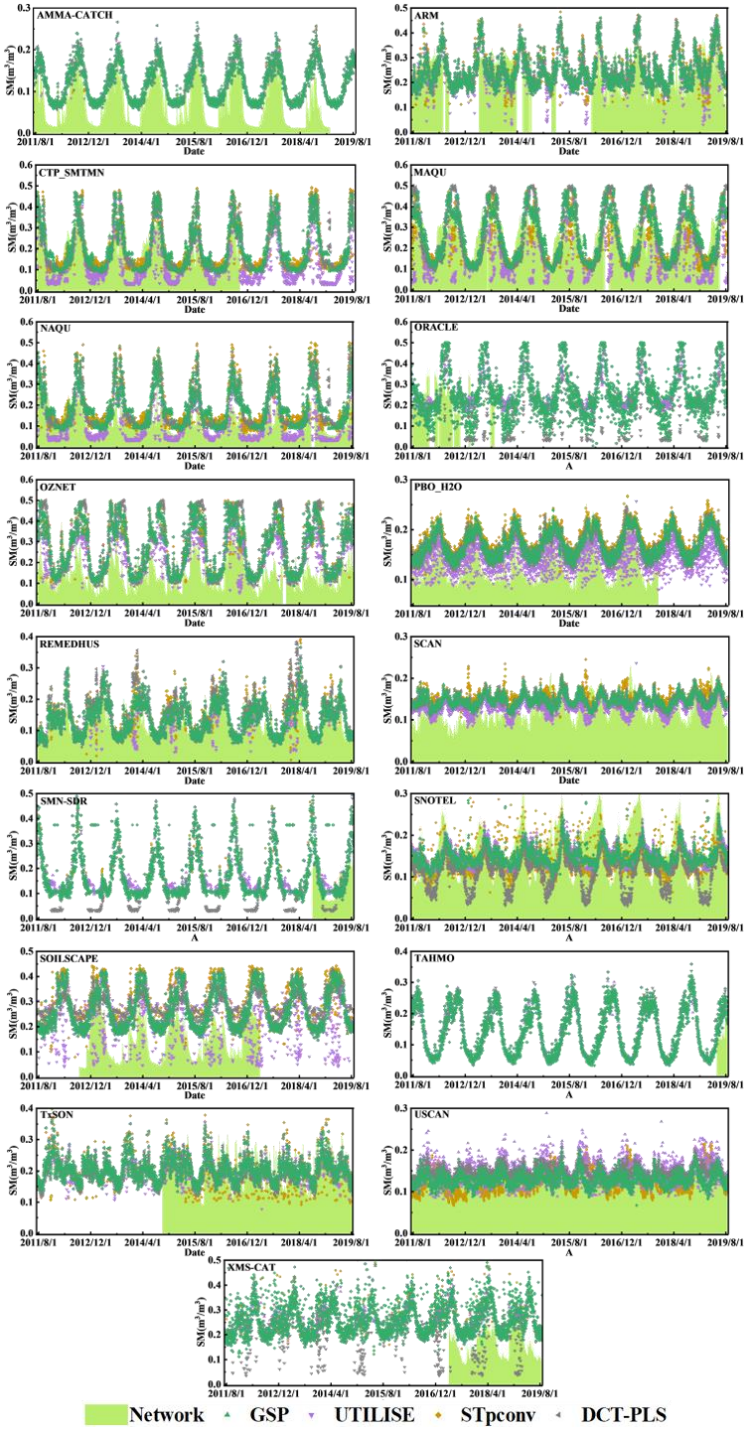

Fig. 5. Temporal profiles of the reconstructed FY-3B SM dataset at the 17 sparse networks

https://doi.org/10.5194/essd-2026-79
Preprint. Discussion started: 24 March 2026

Open Access Earth System Science Data Discussions

(the date format on the x-axis is yyyy/mm/dd).

Table 2

Accuracy evaluation of the reconstructed FY-3B SM dataset at the 17 sparse networks (bolded and underlines values indicate the greatest and second greatest accuracy).

		R	RMSE (m^3/m^3)	MAE (m^3/m^3)	ubRMSE (m^3/m^3)			*R*	RMSE (m^3/m^3)	MAE (m^3/m^3)	ubRMSE (m^3/m^3)
AMMA-CATCH	GSP	0.8000	0.0594	0.0529	**0.0325**	**ARM**	GSP	0.4969	0.0891	0.0727	0.0746
	U-TILISE	0.8017	**0.0585**	**0.0520**	**0.0325**		U-TILISE	0.4378	0.0958	0.0775	0.0839
	STpconv	0.8019	0.0588	0.0524	**0.0325**		STpconv	0.4779	0.0950	0.0772	0.0813
	DCT-PLS	**0.8063**	0.0591	0.0526	**0.0325**		DCT-PLS	**0.5150**	**0.0875**	**0.0714**	**0.0733**
CTP_SMTMN	GSP	0.7433	0.0969	0.0767	0.0791	**MAQU**	GSP	**0.5916**	**0.1246**	**0.0999**	**0.0968**
	U-TILISE	0.6711	0.1149	0.0914	0.0972		U-TILISE	0.4434	0.1596	0.1294	0.1239
	STpconv	0.7379	0.1009	0.0794	0.0841		STpconv	0.5068	0.1344	0.1064	0.1101
	DCT-PLS	**0.7553**	**0.0946**	**0.0740**	**0.0786**		DCT-PLS	0.5509	0.1407	0.1116	0.1149
NAQU	GSP	0.6707	**0.0924**	0.0732	**0.0673**	**ORACLE**	GSP	0.3048	**0.0958**	**0.0769**	**0.0955**
	U-TILISE	0.6017	0.0963	0.0740	0.0841		U-TILISE	0.1443	0.1161	0.0881	0.1147
	STpconv	0.6534	0.1006	0.0757	0.0788		STpconv	0.1984	0.1135	0.0886	0.1131
	DCT-PLS	**0.6811**	0.0928	**0.0708**	0.0705		DCT-PLS	**0.3080**	0.0996	0.0808	0.0995
OZNET	GSP	0.4727	0.1753	0.1420	**0.1172**	**PBO_H2O**	GSP	**0.4689**	0.0991	0.0843	0.0649
	U-TILISE	0.3535	**0.1729**	**0.1365**	0.1355		U-TILISE	0.3201	**0.0949**	**0.0769**	0.0748
	STpconv	0.4385	0.1836	0.1455	0.1307		STpconv	0.4430	0.1040	0.0879	0.0684
	DCT-PLS	**0.4829**	0.1923	0.1541	0.1271		DCT-PLS	0.4342	0.0984	0.0827	0.0672
REMEDHUS	GSP	0.5193	**0.0919**	**0.0772**	**0.0579**	**SCAN**	GSP	**0.4034**	0.0866	0.0725	0.0627
	U-TILISE	0.4180	0.0948	0.0784	0.0634		U-TILISE	0.3103	0.0887	0.0730	0.0693
	STpconv	0.5131	0.0942	0.0785	0.0610		STpconv	0.3130	0.0964	0.0805	0.0712
	DCT-PLS	**0.5871**	0.0944	0.0792	0.0593		DCT-PLS	0.3981	**0.0834**	**0.0700**	**0.0617**
SMN-SDR	GSP	0.5945	**0.0996**	**0.0778**	**0.0720**	**SNOTEL**	GSP	**0.3988**	**0.1271**	**0.1063**	**0.0939**
	U-TILISE	**0.7085**	0.1063	0.0846	0.0752		U-TILISE	0.2958	0.1319	0.1088	0.1048
	STpconv	0.1660	0.1379	0.1018	0.1147		STpconv	0.2759	0.1315	0.1083	0.1037
	DCT-PLS	0.5935	0.1018	0.0801	0.0731		DCT-PLS	0.3452	0.1300	0.1082	0.0975
SOILSCAPE	GSP	0.5864	0.1707	0.1561	0.0787	**TAHMO**	GSP	0.6610	**0.0448**	0.0371	0.0346
	U-TILISE	0.2870	**0.1664**	**0.1468**	0.1157		U-TILISE	0.6505	0.0463	0.0377	0.0356
	STpconv	**0.5925**	0.1814	0.1651	0.0832		STpconv	**0.6640**	0.0449	**0.0368**	**0.0345**
	DCT-PLS	0.5728	0.1681	0.1537	**0.0771**		DCT-PLS	0.6560	0.0460	0.0378	0.0349
TxSON	GSP	**0.4928**	**0.0798**	**0.0682**	**0.0536**	**USCAN**	GSP	**0.3940**	0.0859	0.0749	**0.0525**
	U-TILISE	0.4624	0.0810	0.0687	0.0561		U-TILISE	0.2904	**0.0835**	**0.0708**	0.0609

https://doi.org/10.5194/essd-2026-79
Preprint. Discussion started: 24 March 2026

XMS-CAT	STpconv	0.4343	0.0835	0.0701	0.0597	**Mean**	STpconv	0.3764	0.0879	0.0759	0.0554
	DCT-PLS	0.4882	0.0804	0.0683	0.0548		DCT-PLS	0.3719	0.0851	0.0733	0.0540
	GSP	**0.5583**	**0.1234**	**0.1114**	0.0619		GSP	**0.5387**	**0.1025**	**0.0859**	**0.0703**
	U-TILISE	0.2616	0.1344	0.1172	0.0893		U-TILISE	0.4387	0.1084	0.0889	0.0834
	STpconv	0.4879	0.1335	0.1189	0.0701		STpconv	0.4753	0.1107	0.0911	0.0795
	DCT-PLS	0.5493	0.1254	0.1134	**0.0618**		DCT-PLS	0.5350	0.1047	0.0872	0.0728

Table 3

Accuracy evaluation of the reconstructed FY-3B SM dataset at the five dense networks (bolded and underlined values indicate the greatest and second greatest accuracy).

		R	**RMSE (m^3/m^3)**	**MAE (m^3/m^3)**	**ubRMSE (m^3/m^3)**			***R***	**RMSE (m^3/m^3)**	**MAE (m^3/m^3)**	**ubRMSE (m^3/m^3)**
BIEBRZA_S-1	FY-3B	0.4304	**0.1838**	**0.1677**	**0.0782**	**Ru_CFR**	FY-3B	0.5676	0.0874	0.0709	0.0871
	GSP	0.5039	0.2017	0.1866	0.0800		GSP	**0.5944**	**0.0854**	0.0690	**0.0851**
	U-TILISE	**0.5145**	0.2208	0.1988	0.0972		U-TILISE	0.5777	**0.0854**	0.0690	**0.0851**
	STpconv	0.4770	0.2093	0.1907	0.0874		STpconv	0.5876	0.0860	0.0700	0.0856
	DCT-PLS	0.4719	0.2045	0.1879	0.0826		DCT-PLS	0.5939	**0.0854**	**0.0688**	**0.0851**
SD_DEM	FY-3B	0.3824	0.0545	0.0508	0.0299	**SWEX_POLAND**	FY-3B	**0.7869**	0.1025	0.0819	**0.0740**
	GSP	0.3783	0.0557	0.0521	0.0298		GSP	0.7809	0.1032	0.0828	0.0744
	U-TILISE	**0.3968**	**0.0540**	**0.0505**	**0.0294**		U-TILISE	**0.7869**	0.1025	0.0819	**0.0740**
	STpconv	0.3810	0.0549	0.0513	0.0299		STpconv	0.7837	0.1026	0.0824	0.0742
	DCT-PLS	0.4167	0.0559	0.0521	0.0296		DCT-PLS	0.7831	**0.1012**	**0.0810**	0.0741
VAS	FY-3B	0.7614	**0.0647**	**0.0534**	**0.0445**	**Mean**	FY-3B	0.5858	**0.0986**	**0.0850**	**0.0627**
	GSP	**0.7785**	0.0662	0.0545	0.0462		GSP	0.6072	0.1024	0.0890	0.0631
	U-TILISE	0.7606	0.0657	0.0536	0.0471		U-TILISE	**0.6073**	0.1057	0.0908	0.0666
	STpconv	0.7178	0.0698	0.0574	0.0486		STpconv	0.5894	0.1045	0.0904	0.0652
	DCT-PLS	0.7670	0.0665	0.0549	0.0471		DCT-PLS	0.6065	0.1027	0.0890	0.0637

To validate the reconstructed FY-3B SM datasets under dense *in-situ* networks, the five *in-situ* networks were considered. Additionally, the time series of the original FY-3B SM was included to compare with the reconstructed FY-3B SM dataset. As shown in Fig. 6, the original FY-3B SM shows the greatest consistency with the *in-situ* data. Moreover, compared with other reconstruction methods, the GSP time-series is the closest to the *in-situ* and original FY-3B SM time-series. The quantitative evaluation results based on the dense networks are summarized in Table 3. The original FY-3B SM and GSP-based reconstruction achieve the lowest RMSE, MAE, and ubRMSE among the five dense *in-situ* networks. Compared to U-TILISE, GSP decreases the mean RMSE, MAE, and ubRMSE by 0.0033 m^3/m^3, 0.0018 m^3/m^3, and 0.0035 m^3/m^3, respectively. When compared to STpconv, the corresponding decreases are 0.0021 m^3/m^3, 0.0014 m^3/m^3, and 0.0021 m^3/m^3. Specifically, the GSP-based reconstruction achieves the largest *R* in the

https://doi.org/10.5194/essd-2026-79
Preprint. Discussion started: 24 March 2026

421 SWEX_POLAND (0.7809) and Vas (0.7785).

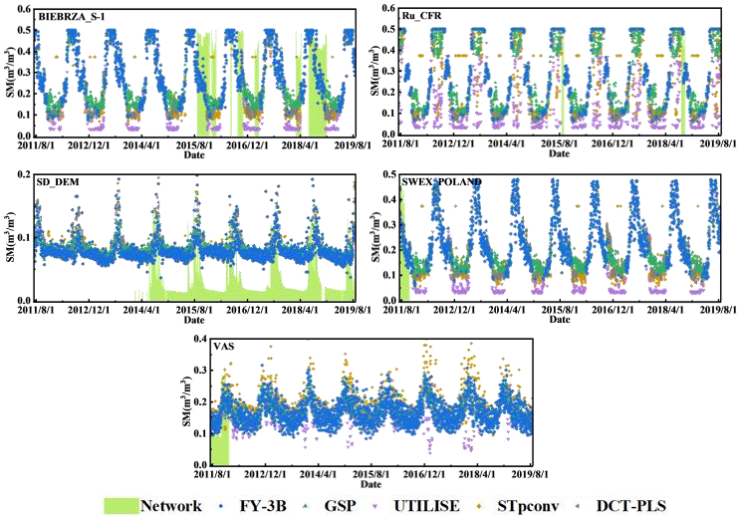

422 **Fig. 6.** Temporal profiles of the reconstructed FY-3B SM dataset at the five dense networks
423 (the date format on the x-axis is yyyy/mm/dd).
424
425

426 *4.2 Validation with original FY-3B SM (simulated gaps)*

427 As mentioned in Section 3.3, simulated gaps were used to evaluate the reconstruction
428 performance of different methods under varying proportions of spatial data missing, where the
429 originally known data were used as a reference for accuracy evaluation. Figs. 7 to 10 present the
430 spatial distribution of both original and reconstructed FY-3B SM under various missing
431 proportions ranging from 30 % to 70 %, with six randomly selected patches illustrated for each
432 scenario. It is noted that the DCT-PLS results are relatively oversmoothed, with visible seams in
433 several areas, such as Patch B2 with the 40 %–50 % missing proportion and Patch C4 with the
434 50 %–60 % missing proportion. Moreover, compared with DCT-PLS, the deep learning-based
435 methods produce more accurate reconstructions, suggesting their ability to exploit
436 spatiotemporally adjacent information, even under spatially large-scale and temporally continuous
437 gaps. Among the methods, the reconstructions based on GSP are the closest to the original FY-3B
438 SM. Table 4 presents the accuracy metrics of the FY-3B SM reconstructed by different methods
439 under varying proportions of spatial missing. Under the 30 %–40 % missing proportion, compared
440 with U-TILISE, STpconv, and DCT-PLS, the MAE of GSP is 0.0018 m ³m ⁻³, 0.0023 m ³m ⁻³, and
441 0.0091 m ³m ⁻³smaller, and the ubRMSE is 0.0050 m ³m ⁻³, 0.0049 m ³m ⁻³, and 0.0127 m ³m ⁻³smaller,
442 correspondingly. When the missing proportion increases to 60 %–70 %, GSP achieves an *R* value
443 of 0.9829, which exceeds those of U-TILISE, STpconv, and DCT-PLS by 0.0118, 0.0152, and
444 0.0612, respectively.

https://doi.org/10.5194/essd-2026-79
Preprint. Discussion started: 24 March 2026

Open Access Earth System Science Data Discussions

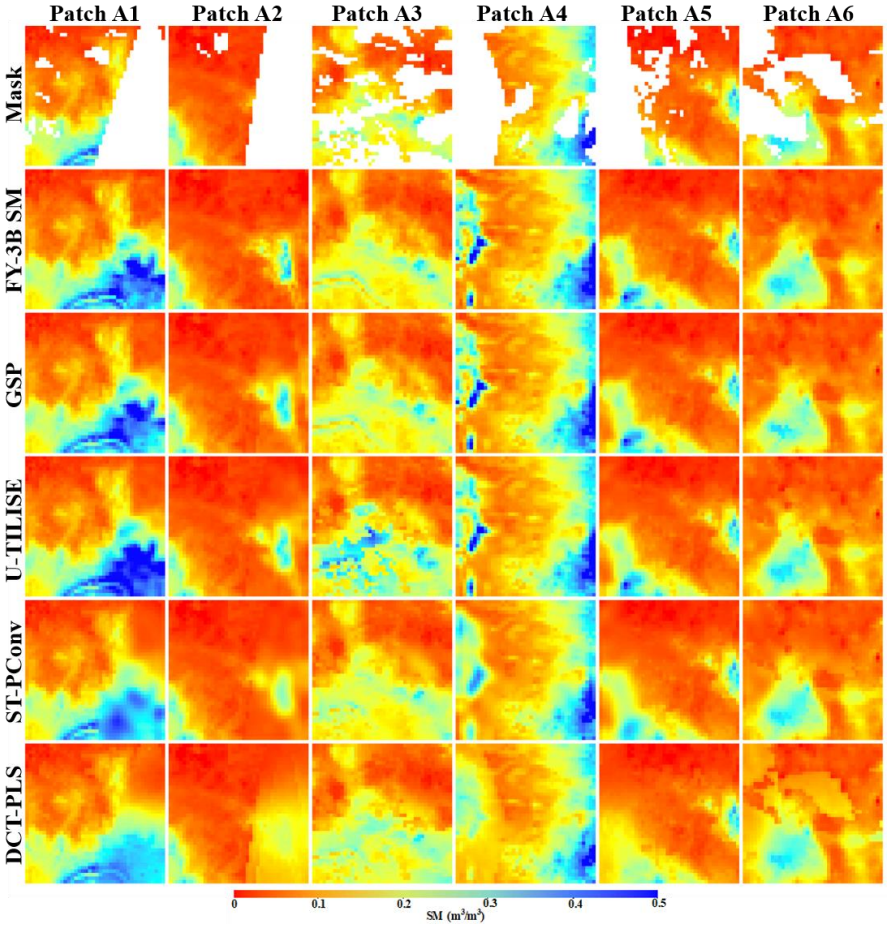

Fig. 7. The reconstructed FY-3B SM with simulated 30 %-40 % missing proportion for six randomly selected patches, with the latitude and longitude of the patch center as: A1 (2017/1/16, 5.5728 °N, 20.5640 °E); A2 (2017/12/12, 9.5122 °N, 27.0716 °E); A3 (2018/1/6, 4.5928 °N, 24.4685 °E); A4 (2018/9/22, 37.4601 °N, 101.7787 °W); A5 (2018/12/24, 8.5238 °N, 25.7701 °E); and A6 (2019/7/31, 11.0997 °S, 32.2777 °E). The first row represents the simulated missing masks for the six patches, and the second to sixth rows represent the original and reconstructed FY-3B SM based on different methods (the date format is yyyy/mm/dd).

https://doi.org/10.5194/essd-2026-79
Preprint. Discussion started: 24 March 2026

Open Access Earth System Science Data Discussions

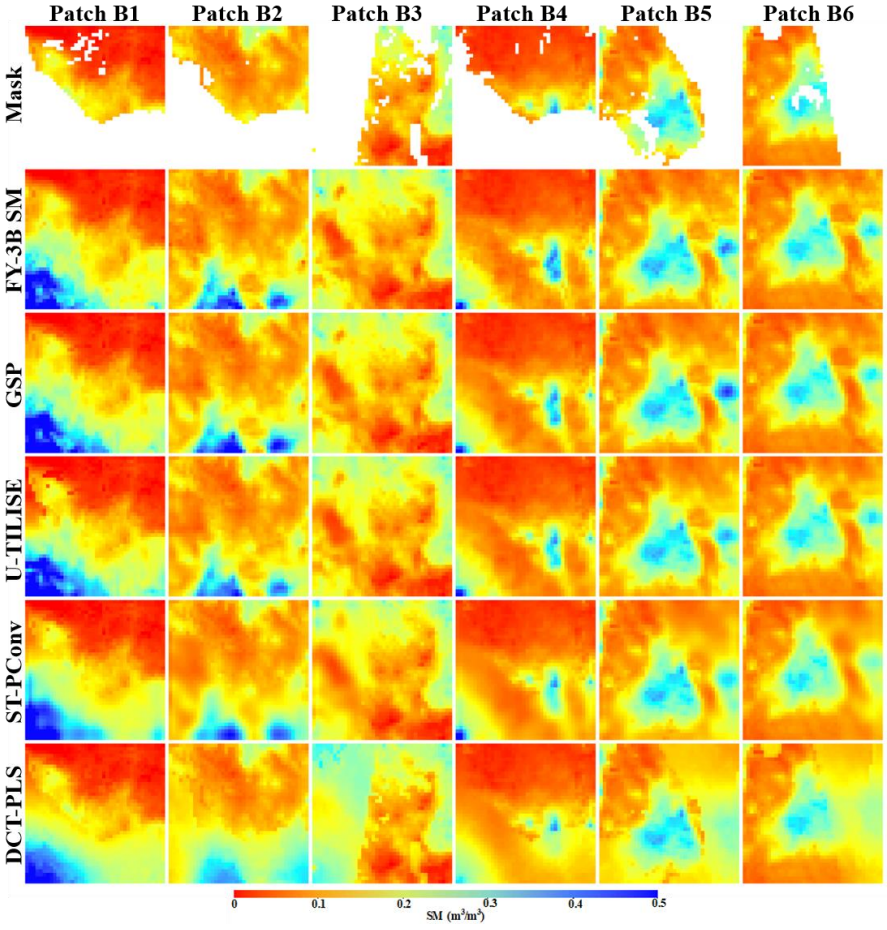

Fig. 8. The reconstructed FY-3B SM with simulated 40 %-50 % missing proportion for six randomly selected patches, with the latitude and longitude of the patch center as: B1 (2017/6/21, 12.4958 °N, 6.7679 °W); B2 (2017/7/3, 9.1165 °S, 20.564 °E); B3 (2017/9/5, 11.0997 °S, 58.8286 °W); B4 (2017/12/7, 9.5122 °N, 28.3731 °E); B5 (2018/7/13, 12.0962 °S, 19.2625 °E); and B6 (2018/7/26, 13.0964 °S, 19.2625 °E). The first row represents the simulated missing masks for the six patches, and the second to sixth rows represent the original and reconstructed FY-3B SM based on different methods (the date format is yyyy/mm/dd).

https://doi.org/10.5194/essd-2026-79
Preprint. Discussion started: 24 March 2026

Open Access Earth System Science Data Discussions

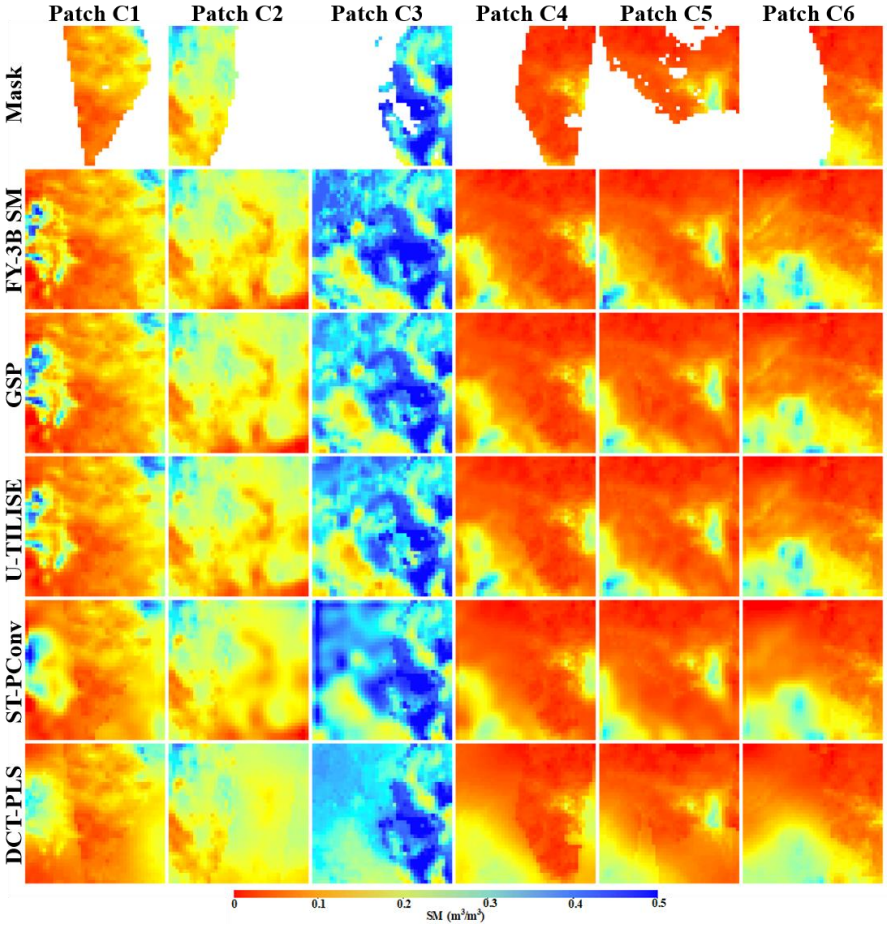

Fig. 9. The reconstructed FY-3B SM with simulated 50 %-60 % missing proportion for six randomly selected patches, with the latitude and longitude of the patch center as: C1 (2017/6/9, 38.7007 °N, 103.0803 °W); C2 (2017/9/12, 10.1066 °S, 57.5271 °W); C3 (2017/10/1, 9.1165 °S, 60.1302 °W); C4 (2017/12/12, 8.5238 °N, 25.7701 °E); C5 (2017/12/25, 8.5238 °N, 27.0716 °E); and C6 (2018/10/30, 9.5122 °N, 23.1672 °E). The first row represents the simulated missing masks for the six patches, and the second to sixth rows represent the original and reconstructed FY-3B SM based on different methods (the date format is yyyy/mm/dd).

https://doi.org/10.5194/essd-2026-79
Preprint. Discussion started: 24 March 2026

Open Access Earth System Science Data Discussions

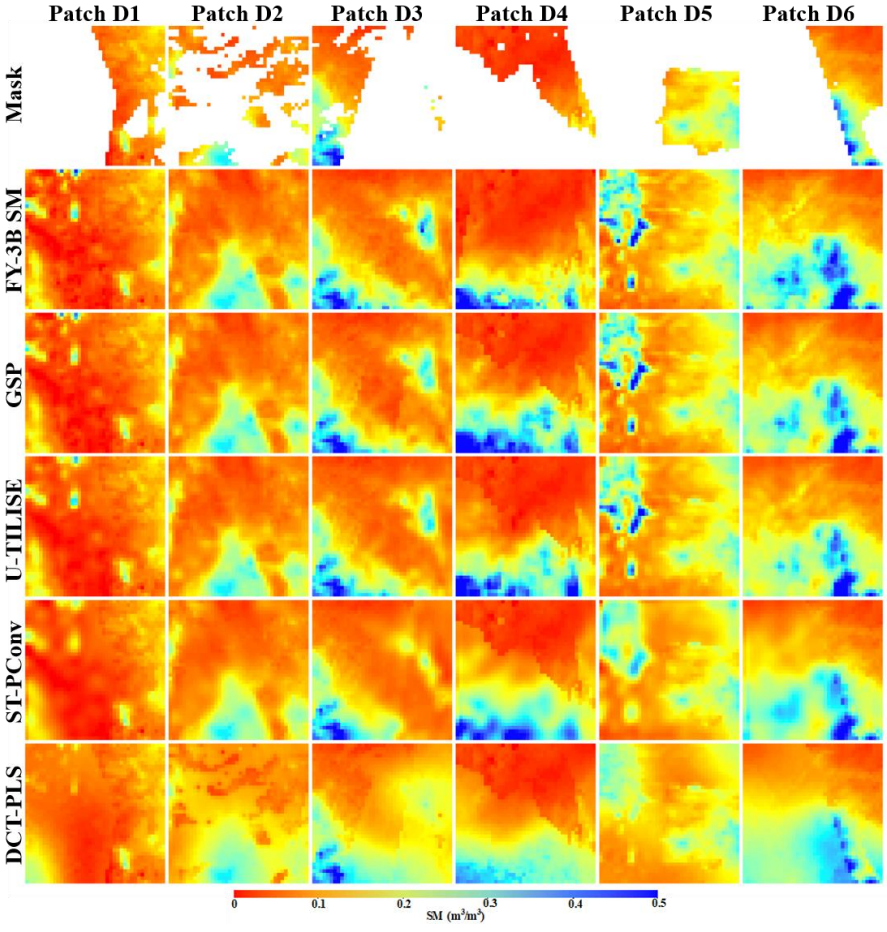

Fig. 10. The reconstructed FY-3B SM with simulated 60 %-70 % missing proportion for six randomly selected patches, with the latitude and longitude of the patch center as: D1 (2017/6/16, 31.5358 °N, 104.3818 °W); D2 (2017/7/29, 13.0964 °S, 19.2625 °E); D3 (2017/12/14, 7.5380 °S, 27.0716 °E); D4 (2018/6/24, 11.4978 °N, 27.0716 °E); D5 (2018/9/28, 36.2407 °N, 130.0803 °W); and D6 (2018/11/13, 8.5238 °N, 20.5640 °E). The first row represents the simulated missing masks for the six patches, and the second to sixth rows represent the original and reconstructed FY-3B SM based on different methods (the date format is yyyy/mm/dd).

https://doi.org/10.5194/essd-2026-79
Preprint. Discussion started: 24 March 2026

Open Access Earth System Science Data Discussions

Table 4

Accuracy of the reconstructed FY-3B SM under different proportions of spatial missing (30 %–70 % in Figs. 7-10).

		R	RMSE (m^3/m^3)	MAE (m^3/m^3)	ubRMSE (m^3/m^3)
30 %-40 %	GSP	**0.9836**	**0.0119**	**0.0073**	**0.0118**
	U-TILISE	0.9668	0.0168	0.0091	0.0168
	ST_PConv	0.9671	0.0167	0.0096	0.0167
	DCT-PLS	0.9275	0.0253	0.0164	0.0245
40 %-50 %	GSP	**0.9837**	**0.0119**	**0.0073**	**0.0119**
	U-TILISE	0.9660	0.0171	0.0091	0.0171
	ST_PConv	0.9686	0.0165	0.0095	0.0164
	DCT-PLS	0.9242	0.0259	0.0167	0.0252
50 %-60 %	GSP	**0.9815**	**0.0121**	**0.0073**	**0.0121**
	U-TILISE	0.9680	0.0159	0.0088	0.0159
	ST_PConv	0.9679	0.0159	0.0094	0.0159
	DCT-PLS	0.9175	0.0261	0.0169	0.0252
60 %-70 %	GSP	**0.9829**	**0.0121**	**0.0073**	**0.0121**
	U-TILISE	0.9711	0.0157	0.0089	0.0157
	ST_PConv	0.9677	0.0166	0.0095	0.0166
	DCT-PLS	0.9217	0.0262	0.0169	0.0255

5. Discussion

5.1 Visualization of the reconstructed dataset at the global scale

Using the GSP-based deep learning framework, this study generated a global, spatially seamless, daily FY-3B SM dataset from 12 July 2011 to 19 August 2019. Fig. 11 shows the original and reconstructed FY-3B SM on five randomly selected dates (i.e., 1 October 2011, 1 August 2013, 1 June 2015, 1 April 2013, and 1 February 2011). Most of the missing regions in the original FY-3B SM are effectively reconstructed, and no noticeable stitching traces are observed in the reconstructed FY-3B SM, indicating great consistency with the original FY-3B SM. Furthermore, Fig. 12 also presents the GSP-reconstructed FY-3B SM for all 30 days of September 2015, where spatial patterns remain stable across days, aligning with the spatiotemporal variability of the original FY-3B SM.

https://doi.org/10.5194/essd-2026-79
Preprint. Discussion started: 24 March 2026

Open Access Earth System Science Data Discussions

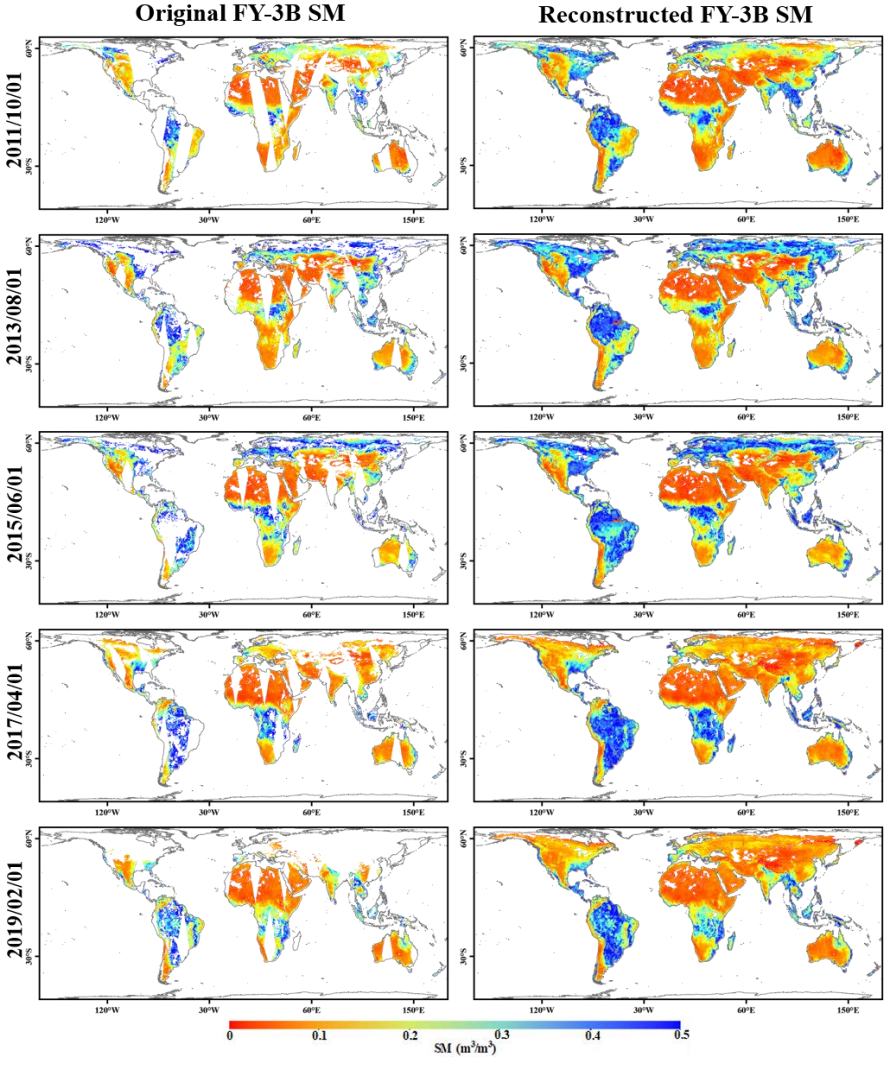

503

504 **Fig. 11.** Original and reconstructed FY-3B SM on five randomly selected dates at the global scale
505 (the date format on the x-axis is yyyy/mm/dd).

https://doi.org/10.5194/essd-2026-79
Preprint. Discussion started: 24 March 2026

Open Access Earth System Science Data Discussions

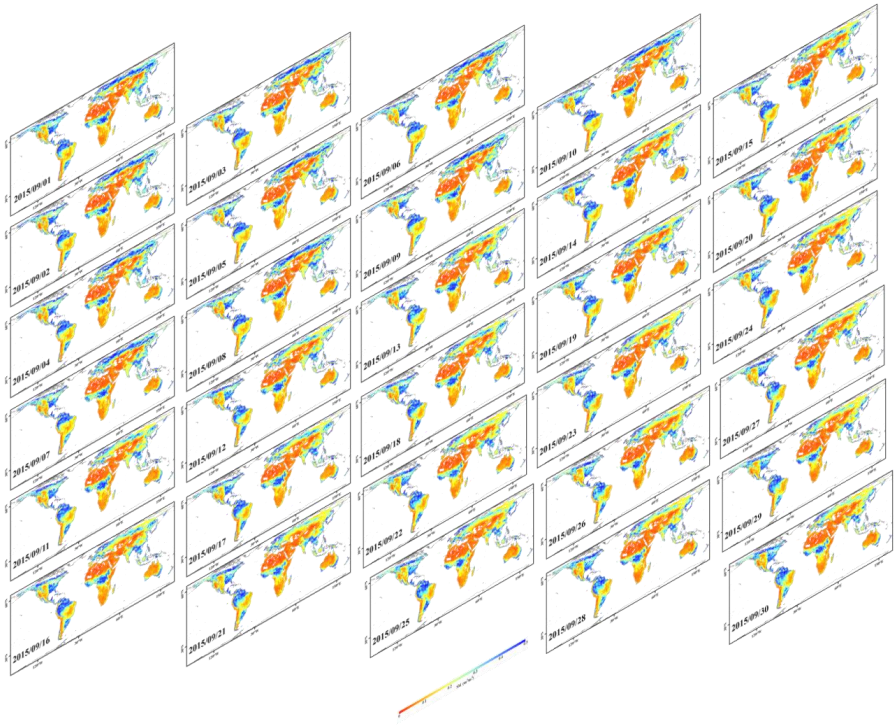

Fig. 12. The GSP reconstructed FY-3B SM in September 2015 (the date format on the x-axis is yyyy/mm/dd).

5.2 Comparison with the TTP-based FY-3B dataset based on in-situ data

To compare the GSP-based FY-3B SM dataset with the previous TTP-based dataset (Wang et al., 2025), *in-situ* data at the station-level were used as reference data for evaluation. The scatter plots between the *in-situ* data and reconstructed datasets are shown in Fig. 13. The GSP-based reconstruction yields lower RMSE, MAE, and ubRMSE than the TTP-based results, with reductions of 0.0060 m^3/m^3, 0.0022 m^3/m^3, and 0.0071 m^3/m^3, respectively. Meanwhile, due to the significant scale differences between *in-situ* data and remote sensing data, the validation strategy based on *in-situ* data suffers from unavoidable uncertainties. Therefore, triple Collocation (TC) was conducted for comparative analysis. The TC method has been widely applied in *in-situ* measurements and satellite observations to assess systematic biases and random errors, providing an evaluation framework for three correlated measurements of the same variable with mutually independent errors. Specifically, TC was applied to the *in-situ* data, the TTP-based FY-3B SM dataset, and the GSP-based FY-3B SM dataset. As shown in Table 5, the *in-situ* data exhibit the lowest *R* and largest RMSE, which is mainly attributed to the large-scale differences between the *in-situ* data and the other two datasets. The reconstructed FY-3B SM dataset based on GSP achieved the greatest accuracy in both metrics, with *R* exceeding that of the TTP-based product by 0.0571 and RMSE lower by 0.0262 m ?m ?

https://doi.org/10.5194/essd-2026-79
Preprint. Discussion started: 24 March 2026

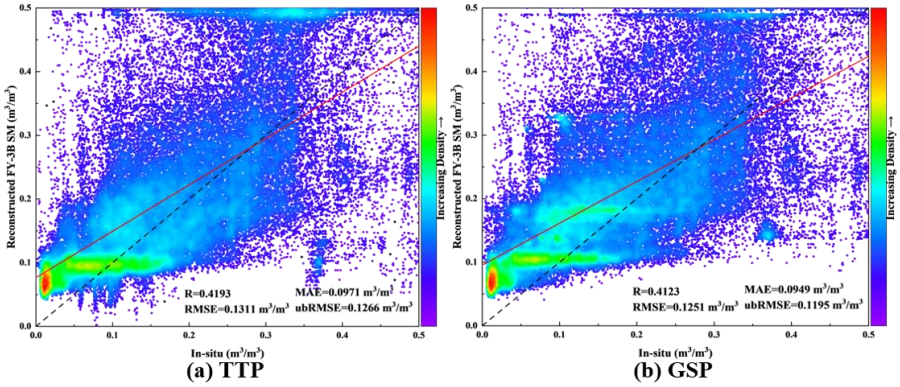

Fig. 13. The scatterplot between the station-level *in-situ* data and reconstructed FY-3B SM.

Table 5

Evaluation based on Triple Collocation.

	R	**RMSE (m^3/m^3)**
In-situ	0.5853	0.0747
TTP	0.9180	0.0472
GSP	**0.9751**	**0.0210**

5.3 Comparison with the TTP-based FY-3B dataset based on GLDAS-Noah data

In contrast to the TTP model, the GSP model further incorporates spatial information, aiming to more effectively exploit surrounding, valid spatiotemporal data to reconstruct accurate FY-3B SM. To further evaluate the reconstruction performance in terms of spatial texture, the Global Land Data Assimilation System-Noah (GLDAS-Noah) with 25 km spatial resolution, which provides spatially complete SM, was adopted as a reference for both qualitative and quantitative analysis. Taking the TTP- and GSP-based data on 16 July 2011 as an example, one region from each of the six continents was randomly selected for visual comparison, as shown in Fig. 14. Generally, the TTP-based FY-3B SM reproduce less spatial texture, while GSP-based results present closer spatial structure to that of GLDAS-Noah, emphasizing the importance of considering spatial information in the FY-3B SM reconstruction. Furthermore, as shown in Table 6, the GSP outperforms TTP in terms of all accuracy metrics, with *R* being 0.0317 larger and ubRMSE being 0.0366 m^3/m^3 lower.

Table 6

Accuracy of the reconstructed FY-3B SM based on TTP and GSP (with the GLDAS-Noah SM as the reference).

	R	**RMSE (m^3/m^3)**	**MAE (m^3/m^3)**	**ubRMSE (m^3/m^3)**
TTP	0.4772	0.1865	0.1591	0.1567
GSP	**0.5089**	**0.1302**	**0.1061**	**0.1201**

https://doi.org/10.5194/essd-2026-79
Preprint. Discussion started: 24 March 2026

Open Access Earth System Science Data Discussions

551

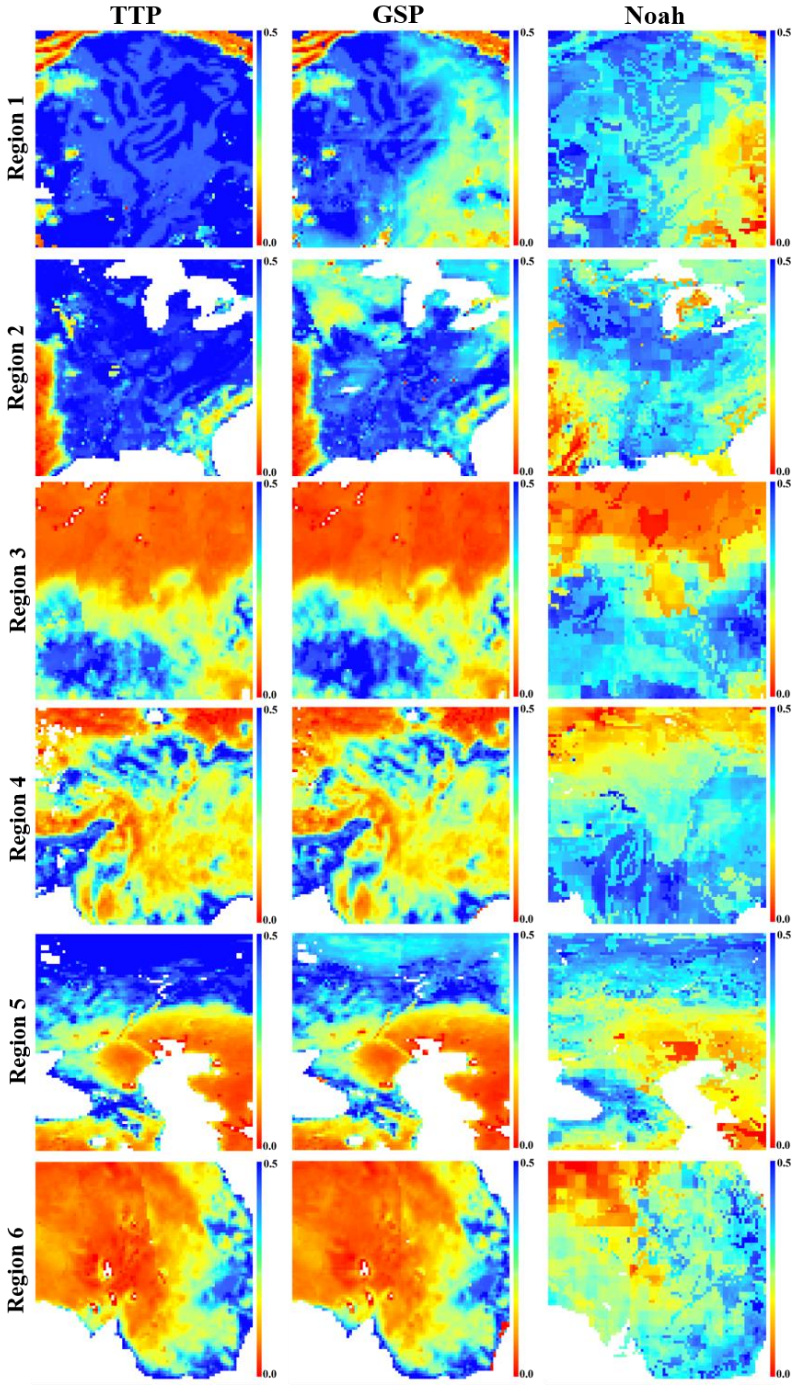

552

553 **Fig. 14.** The spatial texture of TTP- and GSP-reconstructed FY-3B SM datasets and GLDAS-Noah

https://doi.org/10.5194/essd-2026-79
Preprint. Discussion started: 24 March 2026

SM dataset for six randomly selected regions, with the latitude and longitude of the patch center as: Region 1 (4.0054 °S, 67.4187 °W); Region 2 (37.7069 °N, 88.2429 °W); Region 3 (11.6971 °N, 26.2907 °E); Region 4 (28.3807 °N, 99.1757 °E); Region 5 (48.4103 °N, 47.1150 °E); and Region 6 (28.6028 °S, 140.8243 °E).

5.4 Sensitivity analysis based on different climate types

SM controls the distribution of available surface energy and latent heat exchanges, thereby serving as a critical link between the hydrological and energy balances (Li et al., 2024a). This study considers 28 climate types (excluding ET (Tundra) and EF (Ice cap)) to explore the performance of GSP under different climate types. Original FY-3B SM observations from 1 January 2017 to 19 August 2019 were masked randomly (consistent with the steps for constructing the training dataset) to evaluate the accuracy under different climate types. As shown in Table 7, the GSP model maintains stable performances across different climate types, with a mean *R* and RMSE of 0.9496 and 0.0389 m^3/m^3. Among the climate types, the BWh exhibits the greatest accuracy (RMSE=0.0154 m^3/m^3, MAE=0.0117 m^3/m^3, and ubRMSE=0.0118 m^3/m^3), which may be attributed to the absence of vegetation, low precipitation, and reduced atmospheric water vapor, enhancing the reliability of X-band MWRI SM retrieval for the ground measurements, as well as the great surface homogeneity that enhances reconstruction accuracy.

Table 7

Accuracy of the GSP-reconstructed FY-3B SM under different climate types.

	R	**RMSE**	**MAE**	**ubRMSE**
Af	0.9259	0.0419	0.0300	0.0416
Am	0.9384	0.0408	0.0291	0.0407
Aw	0.9643	0.0357	0.0248	0.0355
BWh	0.9333	0.0154	0.0117	0.0118
BWk	0.9395	0.0194	0.0141	0.0164
BSh	0.9691	0.0259	0.0175	0.0251
BSk	0.9558	0.0251	0.0169	0.0240
Csa	0.9480	0.0379	0.0251	0.0369
Csb	0.9595	0.0381	0.0271	0.0373
Csc	0.9140	0.0355	0.0267	0.0350
Cwa	0.9580	0.0361	0.0251	0.0361
Cwb	0.9549	0.0347	0.0246	0.0345
Cwc	0.9233	0.0318	0.0240	0.0298
Cfa	0.9512	0.0390	0.0279	0.0390
Cfb	0.9010	0.0543	0.0364	0.0542
Cfc	0.8910	0.0620	0.0472	0.0609
Dsa	0.9267	0.0216	0.0150	0.0202
Dsb	0.9658	0.0293	0.0196	0.0287
Dsc	0.9674	0.0396	0.0257	0.0393
Dsd	0.8812	0.0638	0.0443	0.0638

https://doi.org/10.5194/essd-2026-79
Preprint. Discussion started: 24 March 2026

Dwa	0.9507	0.0404	0.0271	0.0402
Dwb	0.9562	0.0371	0.0251	0.0369
Dwc	0.9630	0.0388	0.0261	0.0388
Dwd	0.9037	0.0614	0.0427	0.0605
Dfa	0.9389	0.0432	0.0302	0.0432
Dfb	0.9447	0.0427	0.0285	0.0427
Dfc	0.9538	0.0438	0.0283	0.0438
Dfd	0.9288	0.0517	0.0347	0.0517
Mean	0.9496	0.0389	0.0272	0.0381

5.5 Ablation study

To validate the effectiveness of each block and parallel architecture in the GSP model, four ablation experiments were carried out (i.e., 1) with only the multi-scale gated convolution block; 2) with only the residual Swin Transformer block; 3) with the multi-scale gated convolution block and the residual Swin Transformer block in parallel without the CBAM block; and 4) the multi-scale gated convolution block and the residual Swin Transformer block in sequential connection). Table 8 shows the accuracy metrics of the ablation experiments based on the data with simulated gaps from 1 January 2017 to 19 August 2019. Compared with other versions, the GSP model yields consistently greater accuracy. Specifically, the *R* of GSP is 0.0120, 0.0078, 0.0114, and 0.0151 larger than that of versions 1) - 4) respectively. These results demonstrate that each block in the GSP framework contributes positively to the reconstruction of FY-3B SM. Furthermore, compared to sequential connections, the parallel architecture more effectively integrates the features extracted by different blocks.

Table 8

Results of ablation study ("multi-scale Gated Conv + residual Swin Transformer" presents the multi-scale gated convolution block and the residual Swin block in sequential connection).

	R	**RMSE (m^3/m^3)**	**MAE (m^3/m^3)**	**ubRMSE (m^3/m^3)**
multi-scale Gated Conv	0.9707	0.0158	0.0103	0.0158
residual Swin Transformer	0.9749	0.0148	0.0096	0.0148
multi-scale Gated Conv-residual Swin Transformer parallel without the CBAM	0.9713	0.0158	0.0099	0.0158
multi-scale Gated Conv + residual Swin Transformer	0.9676	0.0167	0.0108	0.0167
GSP	**0.9827**	**0.0120**	**0.0073**	**0.0120**

5.6 Future research

We proposed a deep learning model, namely GSP, to reconstruct the global, spatially seamless, daily FY-3B SM dataset from 12 July 2011 to 19 August 2019. The dataset demonstrates reliable accuracy. In the future, the proposed GSP model and the produced dataset can be further

https://doi.org/10.5194/essd-2026-79
Preprint. Discussion started: 24 March 2026

enhanced in several aspects. Firstly, it would be worthwhile to consider fusing multiple heterogeneous auxiliary data, such as precipitation and LST, to fully explore the effective information in the data. Secondly, in terms of network architecture, it is possible to consider combining physical mechanisms (e.g., precipitation event, dry-down events, or $\tau - \omega$ model) with deep learning models to increase the interpretability of the model, such as by imposing constraints on the network architecture or loss function. Finally, it would be interesting to further enhance the spatial resolution of the produced FY-3B SM dataset to support finer-scale applications, including agriculture and water resource management.

6. Data availability

The global, spatially seamless, daily FY-3B SM dataset from 12 July 2011 to 19 August 2019 based on GSP is available at https://doi.org/10.6084/m9.figshare.30633548 (You et al., 2026).

7. Conclusion

In this study, to fill the inherent orbital gaps in the FY-3B SM, the GSP model was proposed to generate a global, spatially seamless, daily FY-3B SM dataset from 12 July 2011 to 19 August 2019. The GSP model takes full advantage of the spatiotemporally adjacent data in the time-series through collaborative local-global feature learning and an adaptive fusion mechanism, harmonizing local detail preservation and global dependency modeling. Specifically, the multi-scale gated convolution block can accurately capture local spatiotemporal features under different receptive fields. The residual Swin Transformer block applies a shifted window strategy to achieve information interaction across multiple windows, thereby learning global spatiotemporal features. Moreover, the CBAM adaptively fuses local and global spatiotemporal features by employing channel and spatial attention mechanisms, enabling the model to focus on critical features.

The *in-situ* data and original FY-3B SM data were used to validate the performance of the GSP model for real and simulated gaps, respectively. In the validation based on the *in-situ* data, we selected 17 sparse networks and five dense networks to evaluate the reconstructed FY-3B SM dataset. Moreover, in the validation based on the original FY-3B SM, to simulate realistic FY-3B SM data gaps, we selected original FY-3B SM orbital gaps with different proportions as masks, and the original SM data were used as a reference for both qualitative and quantitative evaluation. The main conclusions are summarized below:

1) By referring to the sparse and dense *in-situ* networks, the ubRMSE of GSP-reconstructed FY-3B SM dataset is 0.0703 m^3/m^3 and 0.0631 m^3/m^3, respectively, which is more accurate compared to the three benchmark methods (i.e., U-TILISE, STpconv, and DCT-PLS).
2) Based on the station-level *in-situ* data and GLDAS-Noah data, the GSP-reconstructed FY-3B SM dataset exhibits greater accuracy than the recently developed FY-3B SM dataset based on TTP.
3) For simulated gaps, when the spatial missing proportions range from 30 % to 70 %, the reconstructed FY-3B SM based on GSP maintains consistently the greatest accuracy. The GSP method also demonstrates strong robustness, with *R* and RMSE keeping above 0.98

https://doi.org/10.5194/essd-2026-79
Preprint. Discussion started: 24 March 2026

and around 0.0120 m³/m³ respectively.

4) The GSP-reconstructed FY-3B SM dataset demonstrates stable performance across different climate types, with an average MAE of 0.0272 m³/m³ and ubRMSE of 0.0381 m³/m³.

Author contributions

YY designed the research, analyzed the data, wrote the original manuscript, and produced the dataset. QW designed the research, revised the whole manuscript and provided the funding to support the research. RX and XT revised the whole manuscript and provided direction and comments. All the authors edited and approved the final manuscript.

Declaration of Competing Interest

The authors declare that they have no known competing financial interests or personal relationships that could have appeared to influence the work reported in this paper.

Acknowledgments

This work was supported by the National Natural Science Foundation of China under grant Nos. 42221002 and 42222108.

References

Appel, M.: Efficient Data-Driven Gap Filling of Satellite Image Time Series Using Deep Neural Networks with Partial Convolutions, Artificial Intelligence for the Earth Systems, 3, 220055, https://doi.org/10.1175/AIES-D-22-0055.1, 2024.

Bartalis, Z., Wagner, W., Naeimi, V., Hasenauer, S., Scipal, K., Bonekamp, H., Figa, J., and Anderson, C.: Initial soil moisture retrievals from the METOP‐A Advanced Scatterometer (ASCAT), Geophysical Research Letters, 34, http://doi.org/10.1029/2007gl031088, 2007.

Beck, H. E., Zimmermann, N. E., McVicar, T. R., Vergopolan, N., Berg, A., and Wood, E. F.: Present and future Köppen-Geiger climate classification maps at 1-km resolution, Scientific Data, 5, 180214, http://doi.org/10.1038/sdata.2018.214, 2018.

Berg, A. A. and Mulroy, K. A.: Streamflow predictability in the Saskatchewan/Nelson River basin given macroscale estimates of the initial soil moisture status, International Association of Scientific Hydrology Bulletin, 51, 642-654, https://doi.org/10.1623/hysj.51.4.642, 2006.

Chang, Y. L., Liu, Z. Y., Lee, K. Y., and Hsu, W.: Free-Form Video Inpainting With 3D Gated Convolution and Temporal PatchGAN, 2019 IEEE/CVF International Conference on Computer Vision (ICCV), http://doi.org/10.1109/ICCV.2019.00916, 2020.

Cui, C., Xu, J., Zeng, J., Chen, K.-S., Bai, X., Lu, H., Chen, Q., and Zhao, T.: Soil Moisture Mapping from Satellites: An Intercomparison of SMAP, SMOS, FY3B, AMSR2, and ESA CCI over Two Dense Network Regions at Different Spatial Scales, Remote Sensing, 10, http://doi.org/10.3390/rs10010033, 2017.

Dai, P., Ji, S., and Zhang, Y.: Gated Convolutional Networks for Cloud Removal From Bi-Tem

https://doi.org/10.5194/essd-2026-79
Preprint. Discussion started: 24 March 2026

679 poral Remote Sensing Images, Remote Sensing, 12, 3427, https://doi.org/10.3390/rs12203427, 20
680 20.
681 Davidson, M., Attema, E., Snoeij, P., and Levrini, G.: Sentinel-1 Mission Overview and Imple
682 mentation Status, EGU General Assembly Conference Abstracts, http://doi.org/10.1109/IGARSS.2
683 012.6351194, 2009.
684 Dorigo, W., Himmelbauer, I., Aberer, D., and Sabia, R.: The International Soil Moisture Netwo
685 rk: serving Earth system science for over a decade, Hydrology and Earth System Sciences Dis
686 cussions, http://doi.org/10.5194/hess-2021-2, 2021.
687 Dorigo, W. A., Xaver, A., Vreugdenhil, M., Gruber, A., Hegyiová, A., Sanchis-Dufau, A. D., Z
688 amojski, D., Cordes, C., Wagner, W., and Drusch, M.: Global Automated Quality Control of In
689 Situ Soil Moisture Data from the International Soil Moisture Network, Vadose Zone Journal,
690 12, 1-21, http://doi.org/10.2136/vzj2012.0097, 2013.
691 Entekhabi, D., Njoku, E., and O'Neill, P.: The Soil Moisture Active and Passive Mission (SM
692 AP): Science and applications, Radar Conference, 2009, http://doi.org/10.1109/RADAR.2009.497
693 7030, 2009.
694 Fang, K., Shen, C., Kifer, D., and Yang, X.: Prolongation of SMAP to Spatio-temporally Seam
695 less Coverage of Continental US Using a Deep Learning Neural Network, Geophysical Researc
696 h Letters, 44, http://doi.org/10.1002/2017gl075619, 2017.
697 Ford, T. W. and Quiring, S. M.: Comparison of Contemporary In Situ, Model, and Satellite Re
698 mote Sensing Soil Moisture With a Focus on Drought Monitoring, Water Resources Research,
699 55, 1565-1582, https://doi.org/10.1029/2018WR024039, 2019.
700 Geng, X., Li, H., Yao, Z., Chen, X., Yang, Z., Li, S., Wu, L., and Cui, Y.: Potential of ANN
701 for prolonging remote sensing-based soil moisture products for long-term time series analysis,
702 IEEE Geoscience and Remote Sensing Letters, 19, 1-5, http://doi.org/10.1109/LGRS.2021.314011
703 3, 2022.
704 Hegazi, E. H., Yang, L., and Huang, J.: A Convolutional Neural Network Algorithm for Soil
705 Moisture Prediction from Sentinel-1 SAR Images, Remote Sensing, 13, 4964, http://doi.org/10.3
706 390/rs13244964, 2021.
707 Hollinger, J. P., Peirce, J. L., and Poe, G. A.: SSM/I instrument evaluation, IEEE Trans.geosci.
708 remote Sens, 28, 781-790, http://doi.org/10.1109/36.58964, 1991.
709 Jing, W., Zhang, P., and Zhao, X.: Reconstructing Monthly ECV Global Soil Moisture with an
710 Improved Spatial Resolution, Water Resources Management, http://doi.org/10.1007/s11269-018-1
711 944-2, 2018.
712 Kawanishi, T.: The Advanced Microwave Scanning Radiometer for the Earth Observing System
713 (AMSR-E), NASDA's contribution to the EOS for global energy and water cycle studies, Geo
714 science & Remote Sensing IEEE Transactions on, 41, 184-194, http://doi.org/10.1109/TGRS.200
715 2.808331, 2003.
716 Kellogg, K., Hoffman, P., Standley, S., Shaffer, S., and Sarma, C. V. H. S.: NASA-ISRO Synt
717 hetic Aperture Radar (NISAR) Mission, 2020 IEEE Aerospace Conference, http://doi.org/10.110
718 9/AERO47225.2020.9172638, 2020.
719 Kerr, Y. H., Waldteufel, P., Wigneron, J.-P., Delwart, S., Cabot, F., Boutin, J., Escorihuela, M.-
720 J., Font, J., Reul, N., Gruhier, C., Juglea, S. E., Drinkwater, M. R., Hahne, A., Martín-Neira,
721 M., and Mecklenburg, S.: The SMOS Mission: New Tool for Monitoring Key Elements ofthe
722 Global Water Cycle, Proceedings of the IEEE, 98, 666-687, http://doi.org/10.1109/jproc.2010.204

https://doi.org/10.5194/essd-2026-79
Preprint. Discussion started: 24 March 2026

3032, 2010.

Koster, R. D., Dirmeyer, P. A., Guo, Z., Bonan, G., Chan, E., Cox, P., Gordon, C. T., Kanae, S., Kowalczyk, E., Lawrence, D., Liu, P., Lu, C.-H., Malyshev, S., McAvaney, B., Mitchell, K., Mocko, D., Oki, T., Oleson, K., Pitman, A., Sud, Y. C., Taylor, C. M., Verseghy, D., Vasic, R., Xue, Y., and Yamada, T.: Regions of Strong Coupling Between Soil Moisture and Precipitation, Science, 305, 1138-1140, http://doi.org/10.1126/science.1100217, 2004.

Lei, F., Senyurek, V., Kurum, M., Gurbuz, A. C., Boyd, D., Moorhead, R., Crow, W. T., and Eroglu, O.: Quasi-global machine learning-based soil moisture estimates at high spatio-temporal scales using CYGNSS and SMAP observations, Remote Sensing of Environment, 276, http://doi.org/10.1016/j.rse.2022.113041, 2022.

Li, L., Dai, Y., Shangguan, W., Wei, Z., Wei, N., and Li, Q.: Causality-Structured Deep Learning for Soil Moisture Predictions, Journal of Hydrometeorology, 23, 1315-1331, https://doi.org/10.1175/JHM-D-21-0206.1, 2022.

Li, N., Skaggs, T. H., Ellegaard, P., Bernal, A., and Scudiero, E.: Relationships among soil moisture at various depths under diverse climate, land cover and soil texture, Science of The Total Environment, 947, 10, https://doi.org/10.1016/j.scitotenv.2024.174583, 2024a.

Li, Z., Jiang, Y., and Zhao, B.: Abnormal Object Detection System in Cloud Server Centers Based on Transformer, 2024 6th International Conference on Frontier Technologies of Information and Computer (ICFTIC), http://doi.org/10.1109/ICFTIC64248.2024.10913260, 2024.

Li, Z., Stoffelen, A., Verhoef, A., Wang, Z., Shang, J., and Yin, H.: Higher-order calibration on WindRAD (Wind Radar) scatterometer winds, Atmos. Meas. Tech., 16, 4769-4783, http://doi.org/10.5194/amt-16-4769-2023, 2023.

Liu, G., Reda, F. A., Shih, K. J., Wang, T. C., Tao, A., and Catanzaro, B.: Image Inpainting for Irregular Holes Using Partial Convolutions, Springer, Cham, http://doi.org/10.1007/978-3-030-01252-6_6, 2018.

Liu, X., Jiang, L., Wang, G., and Lu, Z.: Downscaling microwave brightness temperatures from FY3B/MWRI with a linear unmixing method, IEEE, http://doi.org/10.1109/IGARSS.2016.7729731, 2016.

Liu, Z., Lin, Y., Cao, Y., Hu, H., Wei, Y., Zhang, Z., Lin, S., and Guo, B.: Swin Transformer: Hierarchical Vision Transformer using Shifted Windows, 2021 IEEE/CVF International Conference on Computer Vision (ICCV), 9992-10002, http://doi.org/10.1109/ICCV48922.2021.00986, 2021.

Llamas, R. M., Guevara, M., Rorabaugh, D., Taufer, M., and Vargas, R.: Spatial Gap-Filling of ESA CCI Satellite-Derived Soil Moisture Based on Geostatistical Techniques and Multiple Regression, Remote Sensing, http://doi.org/10.3390/RS12040665, 2020.

Long, D., Bai, L., Yan, L., Zhang, C. J., and Shi, C.: Generation of spatially complete and daily continuous surface soil moisture of high spatial resolution, Remote Sensing of Environment, 233, https://doi.org/10.1016/j.rse.2019.111364, 2019a.

Long, D., Bai, L., Yan, L., Zhang, C., Yang, W., Lei, H., Quan, J., Meng, X., and Shi, C.: Generation of spatially complete and daily continuous surface soil moisture of high spatial resolution, Remote Sensing of Environment, 233, 111364, https://doi.org/10.1016/j.rse.2019.111364, 2019b.

Njoku, E. G., Stacey, J. M., and Barath, F. T.: The Seasat scanning multichannel microwave radiometer (SMMR): Instrument description and performance, IEEE Journal of Oceanic Engineeri

https://doi.org/10.5194/essd-2026-79
Preprint. Discussion started: 24 March 2026

767 ng, 5, 100-115, http://doi.org/10.1109/OCEANS.1976.1154212, 1980.
768 Owe, M., de Jeu, R., and Holmes, T.: Multisensor historical climatology of satellite - derived g
769 lobal land surface moisture, Journal of Geophysical Research: Earth Surface, 113, http://doi.org/
770 10.1029/2007jf000769, 2008.
771 Parinussa, R., M., Wang, Holmes, T., R. H., Y., Y., Dolman, A., J., Jeu, D., and R., A. M.: G
772 lobal surface soil moisture from the Microwave Radiation Imager onboard the Fengyun-3B sate
773 llite, International Journal of Remote Sensing, https://doi.org/10.1080/01431161.2014.960622, 201
774 4.
775 Parinussa, R., Wang, G., Liu, Y., Hagan, D., and Jeu, R. D.: The Evaluation of Single-Sensor
776 Surface Soil Moisture Anomalies over the Mainland of the People's Republic of China, Remote
777 Sensing, 9, 149, http://doi.org/10.3390/rs9020149, 2017.
778 Parinussa, R. M., Holmes, T. R. H., Wanders, N., Dorigo, W. A., and de Jeu, R. A. M.: A Pr
779 eliminary Study toward Consistent Soil Moisture from AMSR2, Journal of Hydrometeorology, 1
780 6, 932-947, https://doi.org/10.1175/JHM-D-13-0200.1, 2015.
781 Qin, Y., Wu, T., Wu, X., Li, R., Xie, C., Qiao, Y., Hu, G., Zhu, X., Wang, W., and Shang,
782 W.: Assessment of reanalysis soil moisture products in the permafrost regions of the central of
783 the Qinghai–Tibet Plateau, Hydrological Processes, 31, 4647-4659, http://doi.org/10.1002/hyp.11
784 383, 2017.
785 Shangguan, Y., Min, X., and Shi, Z.: Gap Filling of the ESA CCI Soil Moisture Data Using a
786 Spatiotemporal Attention-Based Residual Deep Network, IEEE Journal of Selected Topics in A
787 pplied Earth Observations and Remote Sensing, 16, 5344-5354, http://doi.org/10.1109/JSTARS.20
788 23.3284841, 2023.
789 Shen, H., Li, X., Cheng, Q., Zeng, C., Yang, G., Li, H., and Zhang, L.: Missing Information
790 Reconstruction of Remote Sensing Data: A Technical Review, IEEE Geoscience & Remote Sen
791 sing Magazine, 3, 61-85, http://doi.org/10.1109/mgrs.2015.2441912, 2015.
792 Simpson, J., Kummerow, C., Tao, W. K., and Adler, R. F.: The Tropical Rainfall Measuring M
793 ission (TRMM) Sensor Package, Meteorology & Atmospheric Physics, 60, 19-36, http://doi.org/
794 10.1007/978-3-319-72583-3_6, 1996.
795 Stucker, C., Garnot, V. S. F., and Schindler, K.: U-TILISE: A Sequence-to-Sequence Model for
796 Cloud Removal in Optical Satellite Time Series, IEEE Transactions on Geoscience and Remot
797 er Sensing, 61, 16, http://doi.org/10.1109/TGRS.2023.3333391, 2023.
798 Tang, W., Zhou, J., Ma, J., Wang, Z., Ding, L., Zhang, X., and Zhang, X.: TRIMS LST: a da
799 ily 1km all-weather land surface temperature dataset for China's landmass and surrounding area
800 s (2000–2022), Earth System Science Data Discussions, 16, 33, http://doi.org/10.1109/ICCV5107
801 0.2023.01239, 2024.
802 Tavakol, A., Rahmani, V., Quiring, S. M., and Kumar, S. V.: Evaluation analysis of NASA SM
803 AP L3 and L4 and SPoRT-LIS soil moisture data in the United States, Remote Sensing of En
804 vironment, 229, 234-246, http://doi.org/10.1016/j.rse.2019.05.006, 2019.
805 Wang, G., Garcia, D., Liu, Y., De Jeu, R., and Dolman, A. J.: A three-dimensional gap filling
806 method for large geophysical datasets: Application to global satellite soil moisture observations,
807 Environmental Modelling & Software, 30, 139-142, http://doi.org/10.1016/j.envsoft.2011.10.015,
808 2012.
809 Wang, G., Ma, X., Hagan, D. F. T., Schalie, R. v. d., Kattel, G., Ullah, W., Tao, L., Miao, L.,
810 and Liu, Y.: Towards Consistent Soil Moisture Records from China's FengYun-3 Microwave

https://doi.org/10.5194/essd-2026-79
Preprint. Discussion started: 24 March 2026

811 Observations, Remote Sensing, 14, http://doi.org/10.3390/rs14051225, 2022.
812 Wang, Q., You, Y., Yang, H., Xu, R., Zhang, H. K., Lu, P., and Tong, X.: A TCN-Transforme
813 r Parallel model for reconstruction of a global, daily, spatially seamless FY-3B soil moisture da
814 taset, Remote Sensing of Environment, 328, http://doi.org/10.1016/j.rse.2025.114841, 2025.
815 Wei, Z., Miao, L., Peng, J., Zhao, T., Meng, L., Lu, H., Peng, Z., Cosh, M. H., Fang, B., an
816 d Lakshmi, V.: Bridging spatio-temporal discontinuities in global soil moisture mapping by cou
817 pling physics in deep learning, Remote Sensing of Environment, 313, http://doi.org/10.1016/j.rse.
818 2024.114371, 2024.
819 Woo, S., Park, J., Lee, J. Y., and Kweon, I. S.: CBAM: Convolutional Block Attention Modul
820 e, Springer, Cham, http://doi.org/10.1007/978-3-030-24274-9_20, 2018.
821 Xie, S., Wang, C., Wang, C., Lin, Y., and Dong, X.: Online identification method of tea disea
822 ses in complex natural environments, IEEE Open Journal of the Computer Society, 4, 62-71, ht
823 tp://doi.org/10.1007/978-94-007-0726-9_4, 2023.
824 Xing, C., Chen, N., Zhang, X., and Gong, J.: A Machine Learning Based Reconstruction Meth
825 od for Satellite Remote Sensing of Soil Moisture Images with In Situ Observations, Remote Se
826 nsing, 9, 484, http://doi.org/10.3390/rs9050484, 2017.
827 Xu, X., Hu, J., Yang, J., Ran, Y., and Tan, Z.: A Fish Detection and Tracking Method Based
828 on Improved Interframe Difference and YOLO-CTS, IEEE Transactions on Instrumentation and
829 Measurement, 73, http://doi.org/10.1109/TIM.2024.3476529, 2024.
830 Yang, H., Weng, F., Lv, L., Lu, N., and Xu, H.: The FengYun-3 Microwave Radiation Imager
831 On-Orbit Verification, IEEE Transactions on Geoscience and Remote Sensing, http://doi.org/10.1
832 109/TGRS.2011.2148200, 2011.
833 Yang, Z., Liu, B., Xiong, Y., and Wu, G.: GDB: Gated Convolutions-based Document Binarizat
834 ion, Pattern Recognition, 146, 109989, https://doi.org/10.1016/j.patcog.2023.109989, 2024.
835 You, Y., Wang, Q., Xu, R., and Tong, X.: A global, spatially seamless, daily FY-3B SM datas
836 et from 12 July 2011 to 19 August 2019, Figshare [dataset], https://doi.org/10.6084/m9.figshare.
837 30633548, 2026.
838 Zhang, C., Bai, X., Wang, D., and Zhou, K. X.: Context Aggregation Network for Remote Se
839 nsing Image Semantic Segmentation, International Journal of Computational Intelligence & Appl
840 ications, 23, http://doi.org/10.1142/S1469026824500093, 2024a.
841 Zhang, D., Lu, L., Li, X., Zhang, J., Zhang, S., and Yang, S.: Spatial Downscaling of ESA C
842 CI Soil Moisture Data Based on Deep Learning with an Attention Mechanism, Remote Sensing,
843 16, 27, http://doi.org/10.3390/rs16081394, 2024b.
844 Zhang, G., Hao, Z., Zhu, S., Zhou, C., and Hua, J.: Missing data reconstruction and evaluation
845 of retrieval precision for AMSR2 soil moisture, Transactions of the Chinese Society of Agricu
846 ltural Engineering (Transactions of the CSAE), 32, 137-143, http://doi.org/10.11975/j.issn.1002-6
847 819.2016.20.018, 2016.
848 Zhang, H., Ma, Z., and Li, X.: RS-DETR: An Improved Remote Sensing Object Detection Mo
849 del Based on RT-DETR, Applied Sciences, 14, 10331, http://doi.org/10.3390/app142210331, 202
850 4c.
851 Zhang, Q., Yuan, Q., Jin, T., Song, M., and Sun, F.: SGD-SM 2.0: an improved seamless glob
852 al daily soil moisture long-term dataset from 2002 to 2022, Earth Syst. Sci. Data, 14, 4473-44
853 88, http://doi.org/10.5194/essd-14-4473-2022, 2022.
854 Zhang, Q., Yuan, Q., Li, J., Wang, Y., and Zhang, L.: Generating seamless global daily AMSR

https://doi.org/10.5194/essd-2026-79
Preprint. Discussion started: 24 March 2026

2 soil moisture (SGD-SM) long-term products for the years 2013–2019, Earth System Science Data, 13, 1385-1401, http://doi.org/10.5194/essd-13-1385-2021, 2021.

Zhang, Y., Huang, F., Li, L., Li, Q., Zhang, Y., and Shangguan, W.: Real-Time Forecast of S MAP L3 Soil Moisture Using Spatial–Temporal Deep Learning Model with Data Integration, R emote Sensing, 15, 366, http://doi.org/10.3390/rs15020366, 2023.

Zhu, X. X., Tuia, D., Mou, L., Xia, G. S., Zhang, L., Xu, F., and Fraundorfer, F.: Deep Learn ing in Remote Sensing: A Comprehensive Review and List of Resources, IEEE Geoscience & Remote Sensing Magazine, 5, 8-36, http://doi.org/10.1109/MGRS.2017.2762307, 2018.